the plant journal

The Plant Journal (2021) doi: 10.1111/tpj.15435

The mitochondrial and chloroplast dual targeting of a multifunctional plant viral protein modulates chloroplast-to-nucleus communication, RNA silencing suppressor activity, encapsidation, pathogenesis and tissue tropism

Jose A. Navarro*, Maria Saiz-Bonilla, Jesus A. Sanchez-Navarro and Vicente Pallas*

Department of Molecular and Evolutionary Plant Virology, Institute for Plant Molecular and Cell Biology, Consejo Superior de Investigaciones Científicas-Universitat Politècnica de València, Av. Ingeniero Fausto Elio, Valencia 46022, Spain

Received 29 March 2021; accepted 19 July 2021.
*For correspondence (e-mail janavarr@ibmcp.upv.es; vpallas@ibmcp.upv.es).

SUMMARY

Plant defense against melon necrotic spot virus (MNSV) is triggered by the viral auxiliary replicase p29 that is targeted to mitochondrial membranes causing morphological alterations, oxidative burst and necrosis. Here we show that MNSV coat protein (CP) was also targeted to mitochondria and mitochondrial-derived replication complexes [viral replication factories or complex (VRC)], in close association with p29, in addition to chloroplasts. CP import resulted in the cleavage of the R/arm domain previously implicated in genome binding during encapsidation and RNA silencing suppression (RSS). We also show that CP organelle import inhibition enhanced RSS activity, CP accumulation and VRC biogenesis but resulted in inhibition of systemic spreading, indicating that MNSV whole-plant infection requires CP organelle import. We hypothesize that to alleviate the p29 impact on host physiology, MNSV could moderate its replication and p29 accumulation by regulating CP RSS activity through organelle targeting and, consequently, eluding early-triggered antiviral response. Cellular and molecular events also suggested that S/P domains, which correspond to processed CP in chloroplast stroma or mitochondrion matrix, could mitigate host response inhibiting p29-induced necrosis. S/P deletion mainly resulted in a precarious balance between defense and counter-defense responses, generating either cytopathic alterations and MNSV cell-to-cell movement restriction or some degree of local movement. In addition, local necrosis and defense responses were dampened when RSS activity but not S/P organelle targeting was affected. Based on a robust biochemical and cellular analysis, we established that the mitochondrial and chloroplast dual targeting of MNSV CP profoundly impacts the viral infection cycle.

Keywords: melon necrotic spot virus, chloroplasts, mitochondria, dual targeting, coat protein, silencing, hypersensitive response.

INTRODUCTION

Positive strand RNA plant viruses replicate in the cytoplasm of susceptible cells over or within specialized membranous compartments named viral replication factories or complexes (VRCs). VRCs are supposed to concentrate viral and host factors, generate a favorable environment for efficient replication and assembly, and protect RNA intermediates against host antiviral mechanisms such as RNA silencing (Laliberté and Sanfaçon, 2010). Besides, a growing body of evidence supports the VRC role in intra- and intercellular movement and long-distance transport through vascular tissues (Laliberté and Zheng, 2014; Wan et al., 2015). It is still unclear how plant viruses orchestrate VRC scaffolding. Nevertheless, it is known that the alteration of membrane morphology is usually triggered by specific organelle targeting of viral proteins, most often those related to replication (Jin et al., 2018). Once there, these proteins establish a network of interactions among other viral and host components, which are then incorporated into VRCs (Nagy, 2016).

Upon building these factories, viruses cause a profound remodeling and proliferation of host cell endomembranes and cytoskeleton, undermining the integrity and function of different organelles. Among them are chloroplasts, mitochondria and peroxisomes, which contribute to maintaining the cellular homeostasis of signaling molecules

such as reactive oxygen species (ROS) and phytohormones, and the endoplasmic reticulum (ER), which is a major protein folding compartment that bears the burden of new viral client proteins (Hernández et al., 2016; Li et al., 2016; Loebenstein, 2009; Su et al., 2019; Verchot, 2016; Zhao et al., 2016). Therefore, the impact of virus replication on organelle function together with viral protein accumulation could result in ROS or misfolded proteins exceeding normal levels. This late event eventually leads to ER stress, altered gene expression and even hypersensitive response (HR)-related cell death (van Aken and van Breusegem, 2015; Pallas and García, 2011). Plant viruses as biotrophic parasites must reverse this adverse situation to preserve cell viability and generate compatible or tolerant interactions. Thus, they have co-evolved a diversity of mechanisms to moderate their harmful effects on the host, not only including counter defense measures, such as suppression of RNA silencing, or inhibition of both oxidative burst and expression of plant innate immunity-associated genes, but also self-attenuating their replication (Paudel and Sanfaçon, 2018).

Viral replication factories or complex architecture and biogenesis have been mainly studied in members of the families Tombusviridae and Potyviridae (Jin et al., 2018). Cytopathology studies by transmission electron microscopy showed that melon necrotic spot virus (MNSV) infection deeply modified the structure of mitochondria in melon, enlarging them and inducing big inner dilations as well as multi-vesiculation of the external and surrounding-dilation membranes (Gomez-Aix et al., 2015). These altered mitochondria were frequently localized near plasmodesmata, indicating that they could play a role in the viral spread, always associated with the ER, lipid bodies or droplets. Positive-sense viral RNAs, coat protein (CP) and replicative RNA intermediates (dsRNAs) were mainly detected in big inner dilations, supporting the view that altered mitochondria constitute VRCs. In *Nicotiana benthamiana*, MNSV p29 auxiliary replicase was shown to associate with mitochondrial membranes upon an ectopic (Gomez-Aix et al., 2015) or heterologous viral expression (Mochizuki et al., 2009). Once there, p29 caused VRC-like modification of mitochondrial ultrastructure, loss of mitochondrial membrane potential and necrosis, indicating a role for p29 in VRC formation and, probably, ROS activation of plant defense responses as described for cucumber necrosis virus (CNV) p33 (Rochon et al., 2014).

Previous works by us and others showed that an oxidative burst accompanied melon response to MNSV infection. Briefly, hydrogen peroxide accumulation, which indicates mitochondrial damage, and cell wall fortification by callose deposition was found in local and systemic MNSV necrotic lesions (Fernández-Crespo et al., 2017). Transcriptomic profiling of MNSV local infection unveiled deregulation of genes involved in defense response and oxidative stress (Gómez-Aix et al., 2016). Comparative proteomic analysis of melon phloem exudates in response to MNSV infection revealed that differentially accumulated proteins were mainly involved in controlling redox balance and cell death, for example, an hsr203J HR marker-like carboxylesterase was up-accumulated, suggesting that HR could be activated (Serra-Soriano et al., 2015). Jasmonic acid (JA) and salicylic acid (SA) are antagonistic phytohormones activated simultaneously in the same plants only in the case of effector-triggered immunity (ETI; Betsuyaku et al., 2018). Interestingly, SA, JA precursor 12-oxo-phytodienoic acid, antioxidant ferulic acid and detoxifying glutathione S-transferase mRNA levels increased during the basal response of melon to MNSV, a plant response that was accentuated during hexanoic-primed systemic resistance (Fernández-Crespo et al., 2017).

Systemic lethal necrosis, frequently observed in infection of MNSV family-related tombusviruses, was shown to be induced by auxiliary replicase with the indirect assistance of p19 suppressing plant defense mechanisms (Burgyán et al., 2000). Similarly, the appearance of necrotic symptoms on melon cotyledons was enhanced by MNSV CP, which takes the role of p19 in RNA silencing suppression (RSS) by increasing viral movement (Genoves et al., 2006; Serra-Soriano et al., 2017). MNSV CP consists of three major domains: a disordered N-terminal RNA-binding domain (R-domain), connected to the shell domain (S-domain) by a short and flexible arm, and the protruding domain (P-domain). Each domain plays different roles during infection, making MNSV CP an exceptional multifunctional protein. The R domain and the arm region are required for genome interaction and encapsidation, siRNA binding and suppression of RNA silencing, the S domain has a structural function, whereas the P domain is involved in compatibility with fungus vector zoospores (Genoves et al., 2006; Ohki et al., 2010; Serra-Soriano et al., 2017). MNSV CP also works as a host determinant as CP from melon isolates allows watermelon isolates to infect melon locally (Ohki et al., 2008). Despite all this information, studies about CP subcellular localization, which are limited to the immunolocalizations mentioned above, and underlying molecular determinants are still lacking. Here we show that the R/arm region can act as an ambiguous transit peptide driving dual targeting of MNSV CP to mitochondria and chloroplasts in ectopic expression and during MNSV infection. CP was additionally found in altered mitochondria, resembling VRCs that moved along the cellular periphery of infected cells, supporting a link between intracellular movement and replication. We also evaluated the role of p29 in VRC biogenesis showing cellular events not previously described. Before necrosis appearance, ectopically expressed p29 was located around mitochondria displaying a swollen morphology and forming small ER-associated groups together with large juxtanuclear

clusters. Based on cellular features, the effect of different CP mutations on MNSV infectivity, and expression levels of HR, defense and oxidative stress-related host genes, we propose new functions for MNSV CP, associated with its organelle targeting, in managing the balance between plant defense and virus counter-defense responses.

RESULTS

Transiently expressed MNSV CP has a dual localization to chloroplasts and mitochondria

To study MNSV CP subcellular localization in plant cells, the green fluorescent protein (GFP) was fused to its C- or N-terminus (CP-GFP and GFP-CP, respectively) and transiently expressed in *N. benthamiana* leaves. The fluorescence, visualized under confocal laser-scanning microscopy (CLSM) at 48 h post-infiltration (hpi), was mainly found in chloroplasts, as shown by the superposition of GFP and chlorophyll fluorescence, and in small and motile punctate bodies (Figure 1a; Movie S1) that overlapped with coxP-ChFP, a mitochondrial matrix marker (Figure 1b). Chloroplast-associated CP-GFP fluorescence was mainly observed in the stroma as revealed by its colocalization with NRIP1-ChFP, a stromal component (Caplan et al., 2008; Figure 1c), but not with CHUP1-ChFP, a chloroplast outer envelope protein (Oikawa et al., 2008; Figure 1d). Consistent with stromal localization, CP-GFP fluorescence was also detected in stromules (Figure 1e, up). Furthermore, CP-GFP fluorescence was frequently observed, forming discrete spots around chlorophyll fluorescence as described for CNV CP (Figure 1e, down). We found that these structures colocalized with the magnesium-protoporphyrin IX chelatase H subunit (CHLH/ABAR), a spanning chloroplast envelope receptor of ABA (Shang et al., 2010) and tetrapyrrole sensor, which mediates plastid-to-nucleus retrograde signaling (Figure 1f; Nott et al., 2006). It has been reported that this pattern might result from the over-accumulation of chloroplast-targeted proteins that are prone to aggregate, such as viral CPs do (Chaudhary and Yadav, 2019; Perello et al., 2016). In contrast, cells expressing GFP-CP showed nucleo-cytoplasmic fluorescence distribution (Figure 1g). It is known that the fusion of tags to the N-terminus of the protein of interest interferes with plastid and mitochondrial localization

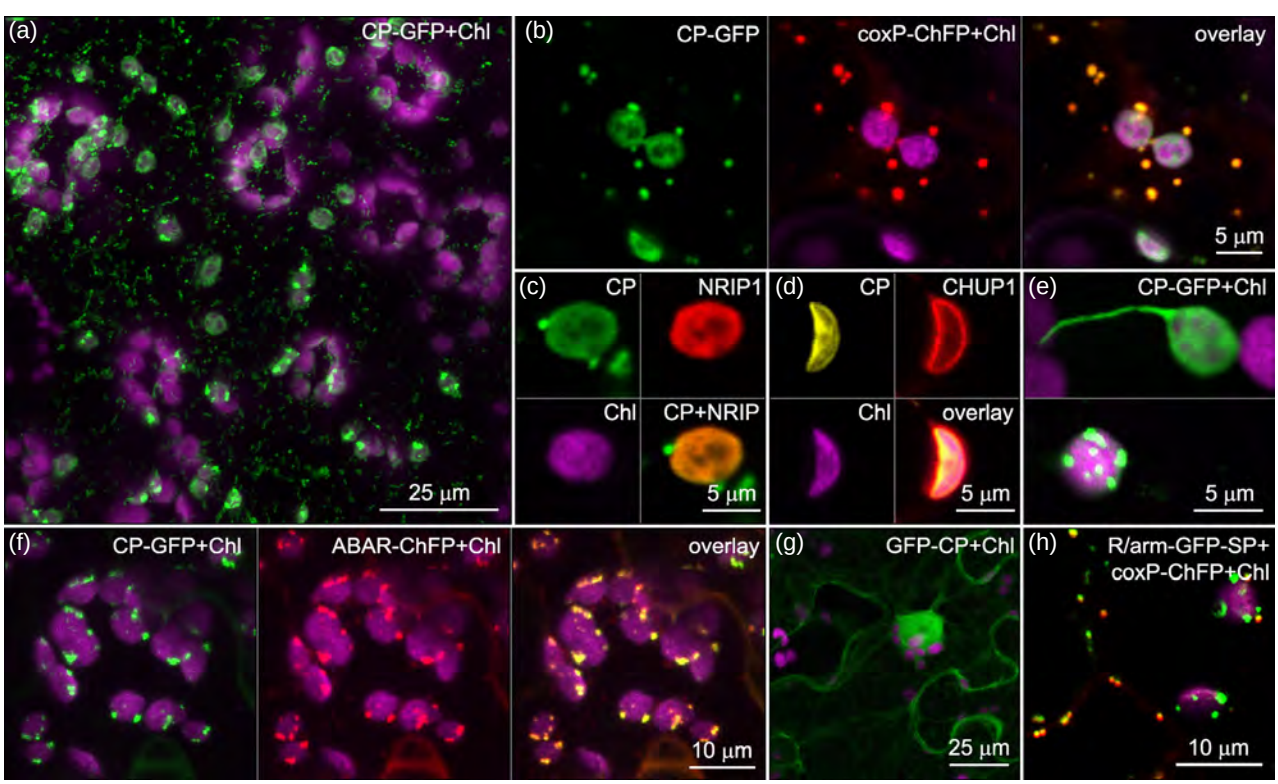

Figure 1. Subcellular localization of green fluorescent protein (GFP)-tagged coat protein (CP) upon transient expression in *Nicotiana benthamiana* leaves.
(a) Z-stack projection showing CP-GFP distribution in epidermal and mesophyll cells.
(b) Co-expression of CP-GFP and the mitochondrial matrix marker, coxP-ChFP.
(c,d) Image of a CP-GFP-labeled chloroplast expressing the stromal, NRIP1-ChFP (c), or outer-envelope, CHUP1-ChFP (d), proteins.
(e) CP-GFP-labeled chloroplast showing a stromule (up) or envelope-associated spots (down).
(f) Co-expression of CP-GFP and CHLH/ABAR-ChFP.
(g) GFP-CP nucleo-cytoplasmic distribution in epidermal cells.
(h) Co-expression of R/arm-GFP-SP and coxP-ChFP. Images correspond to single scans unless indicated. Chl, chlorophyll autofluorescence in magenta.

signals, which are mainly located at this protein end. To solve this issue, an internally GFP-tagged CP was constructed by inserting the fluorescent protein between the arm region and the S domain (R/arm-GFP-SP). This fusion protein has the advantage that the putative targeting signals present at the N- and C-terminus of the CP are not masked by the tag (Tanz et al., 2013). After co-expression with coxP-ChFP, R/arm-GFP-SP showed a fluorescent pattern similar to that described above for CP-GFP, labelling mitochondria, chloroplasts and chloroplast envelope-associated spots (Figure 1h). Therefore, CP-GFP and R/arm-GFP-SP reflect more accurately the actual subcellular localization of the CP than GFP-CP, revealing the presence of a dual-targeting signal at the N-terminus of the CP.

The N-terminal R/arm domain drives CP mitochondrial and chloroplast dual targeting, and induces chloroplast-to-nucleus communication through stromule extension

Although MNSV has been classified into the genus *Gammacarmovirus*, its CP shows a high degree of similarity to CPs in the genus *Tombusvirus* (Riviere et al., 1989; Wada et al., 2008). CPs from 16 out of 17 tombusviruses and MNSV CP were predicted to target chloroplasts and/or mitochondria by WoLF PSORT, LOCALIZER and YLOC (Briesemeister et al., 2010; Horton et al., 2007; Sperschneider et al., 2017; Table S2). Accordingly, the N-terminal 39 amino acids of the CNV CP R domain were sufficient for mitochondrial import, whereas the arm region plus the first four aa (SVRI motif) of the S domain were required for chloroplast targeting (Hui et al., 2010; Xiang et al., 2006). To reinforce this notion, we analyzed five tombusvirus CPs for their subcellular localization by using C-terminal GFP fusions. Except for tomato bushy stunt virus CP, the carnation Italian ringspot virus, cymbidium ringspot virus, Neckar river virus and pelargonium necrotic spot virus CPs were localized in chloroplasts and mitochondria (Figure S1). In contrast to MNSV CP, some of these tombusvirus CPs also showed a high degree of cytoplasmic localization. This result is consistent with previous work about CNV CP reporting that only 1–5% of this protein is targeted to chloroplast during infection (Xiang et al., 2006). Alignment of the tombusvirus and MNSV N-terminal CP sequences showed that an asparagine/arginine-rich stretch at the protein start including an alanine residue at position 2, frequently found in dual (dTP) and chloroplast (cTP) transit peptides (Pujol et al., 2007), was the most conserved region in the R domain (Figure S2). Despite sequence variability, two adjacent alpha-helix (H1 and H2) were always predicted by JPred 4 (Drozdetskiy et al., 2015). Though cTPs usually are unstructured regions, they can form helices in membrane-mimetic environments. Some of these helices showed amphipathic properties, a mitochondrial transit peptide (mTP) typical feature, as calculated by HeliQuest (Gautier et al., 2008; Ge et al., 2014). The arm region was more conserved than the R domain, but the SVRI motif embedded at the beginning of the S domain was only found in the Havel river virus and MNSV (SVKI). Instead, a GSVTV motif was mainly observed among the aligned sequences.

Considering the above-shared features, we examined the role of the MNSV CP N-terminal region in organelle import. We transiently expressed R/arm-GFP, which includes R and arm domains of the MNSV CP, and R/arm/S_{19}-GFP, which also covers the first 19 aa of the S domain, including the SVKI motif and a 14-3-3 chaperone binding like-domain (RX^npSXP; Xiang et al., 2006; Figures S2 and S3). Fluorescence distribution revealed that S domain sequences were not required for transport as both proteins were efficiently targeted to both organelles and additionally to nucleoli (Figure 2a–c). Chloroplast peripherally located spots were not observed, but a high number of chloroplasts extended stromules and, frequently, they were found in perinuclear clusters tightly embracing nuclei through stromules that extend and coil around (Figure 2d–f). To determine the extent of stromule induction, we co-expressed NRIP-ChFP with CP-GFP, R/arm-GFP and glyrsP-GFP, a dual mitochondrial and chloroplast marker used for steady-state control (Duchêne et al., 2001), and quantified the percentage of chloroplasts with NRIP-ChFP-labeled stromules. As expected, the percentage increased with the presence of R/arm-GFP (28.8%, $t = 6.0$ and $P = 0.0002$) compared with control (10.3%). Stromule induction also occurs, but to a lesser extent, with CP-GFP (19.0%, $t = 4.4$ and $P = 0.00006$; Figure 2g).

Chloroplast perinuclear clustering and stromule induction appear to be a general response upon plant pathogen perception in *N. benthamiana*, and could be elicited by ROS (Ding et al., 2019; Krenz et al., 2012). Besides, stromules have been shown to facilitate chloroplastic NRIP1 and ROS transport to the nucleus during ETI induced by the helicase domain (p50) of the tobacco mosaic virus replicase, activating defense responses (Hanson and Hines, 2018). To examine whether stromule induction by R/arm-GFP is also accompanied by retrograde chloroplast-to-nucleus communication, we used a well-established approach based on the fusion of a nuclear export signal (NES) to NRIP1-ChFP N-terminus ($_{NES}$NRIP-ChFP). Therefore, $_{NES}$NRIP-ChFP nuclear localization is only possible when it travels through stromules from the chloroplast where both N-terminal transit peptide and NES are cleaved (Caplan et al., 2015). CLSM analysis at 48 hpi revealed that, in addition to chloroplasts, $_{NES}$NRIP1-ChFP fluorescence was observed in the nucleus and cytoplasm when expressing with R/arm-GFP (Figure 2h) but not CP-GFP (Figure 2i), nor other controls such as GFP, CPΔ(R/arm)-GFP and glyrsP-GFP (Figure S4).

Dissecting R/arm domains reveals that the R_1 subdomain is required but not sufficient for dual targeting

To further define the sequences involved in CP targeting, we performed fine mapping of the R/arm domains by

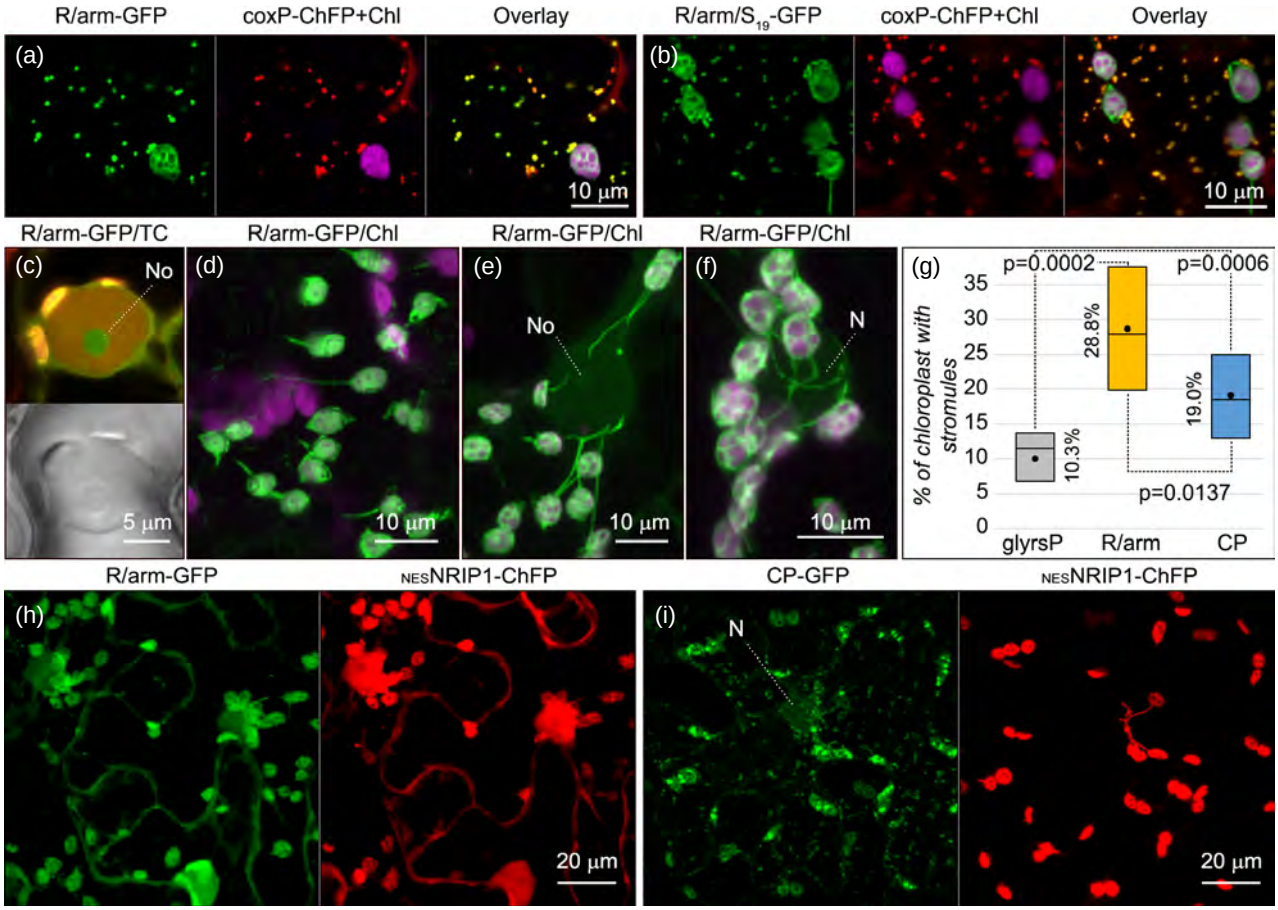

Figure 2. R/arm domain induces chloroplast stromule extension towards nucleus leading to chloroplast-to-nucleus communication.
(a,b) Single scan images showing R/arm-GFP (a) and R/arm/S_{19}-GFP (b) in chloroplasts (Chl, magenta) and mitochondria (coxP-ChFP).
(c) Single scan image showing R/arm-GFP in the nucleolus (up) and the corresponding transmitted channel, TC (down).
(d–f) Confocal laser-scanning microscopy (CLSM) images showing R/arm-GFP in chloroplast and stromules over the cytoplasm (d), near (e) and around (f) the nucleus, N.
(g) Boxplot showing the percentage of NRIP-labeled chloroplasts with stromules in the presence of glyrsP-GFP, R/arm-GFP and CP-GFP from three biological replicates. The lower and upper limits of the boxes are plotting the min and max values, respectively, whereas the lines dividing them represent the median values. Points inside boxes represent the mean from the three replicates, $P < 0.05$ indicates statistical significance.
(h–i) Co-expression of $_{NES}$NRIP1-ChFP with R/arm-GFP (h) or CP-GFP (i). Accumulation of $_{NES}$NRIP1-ChFP in the nucleus was higher upon R/arm-GFP than CP-GFP expression. Chl, chlorophyll autofluorescence in magenta. No, nucleolus. N, nucleus. Images correspond to Z-stack projections unless indicated. CP, coat protein; GFP, green fluorescent protein.

deletion analysis (Figure S3). Either removal of both the R and arm domains in CPΔ(R/arm)-GFP or only the R domain in CPΔR-GFP completely abolished organelle targeting of both proteins that, instead, showed a nucleo-cytoplasmic localization (Figure 3a,b). Though some cytoplasmic background was observed, arm deletion in CPΔarm-GFP did not affect dual import (Figure 3c). Within the R domain, the amino acid composition of the first 30 positions is enriched in basic, hydrophobic and proline residues. In contrast, acidic or helix breaker glycine residues are lacking (Figure S5), which matches with that described for dTPs (Ge et al., 2014). Interestingly, asparagine instead of serine is also overrepresented. The next 30 positions in the R domain or those in the arm region show a more diverse composition. Therefore, we defined two R subdomains (R_1 and R_2) of 30 aa, including H1 and H2, respectively (Figure S2). Other mutants were generated by deleting each R subdomain either alone, CPΔR_1-GFP and CPΔR_2-GFP, or in combination with the arm region, CPΔ(R_1/arm)-GFP and CPΔ(R_2/arm)-GFP (Figure S3). CLSM analysis revealed that CPΔR_1-GFP, CPΔ(R_1/arm)-GFP and CPΔ(R_2/arm)-GFP showed a nucleo-cytoplasmic localization (Figure 3d,f,g, respectively). Small bodies, which did not colocalize with coxP-ChFP, were occasionally observed in some cells expressing CPΔR_1-GFP (Figure 3d, arrows). Proper import to mitochondria and chloroplasts was neither affected in CPΔR_2-GFP, except for some cytoplasmic background (Figure 3e). The same result was observed in CP(R_{81}A)-GFP harboring R_{81}A mutation, which reduces CP RSS capacity (Serra-Soriano et al., 2017; Figure 3h). As expected,

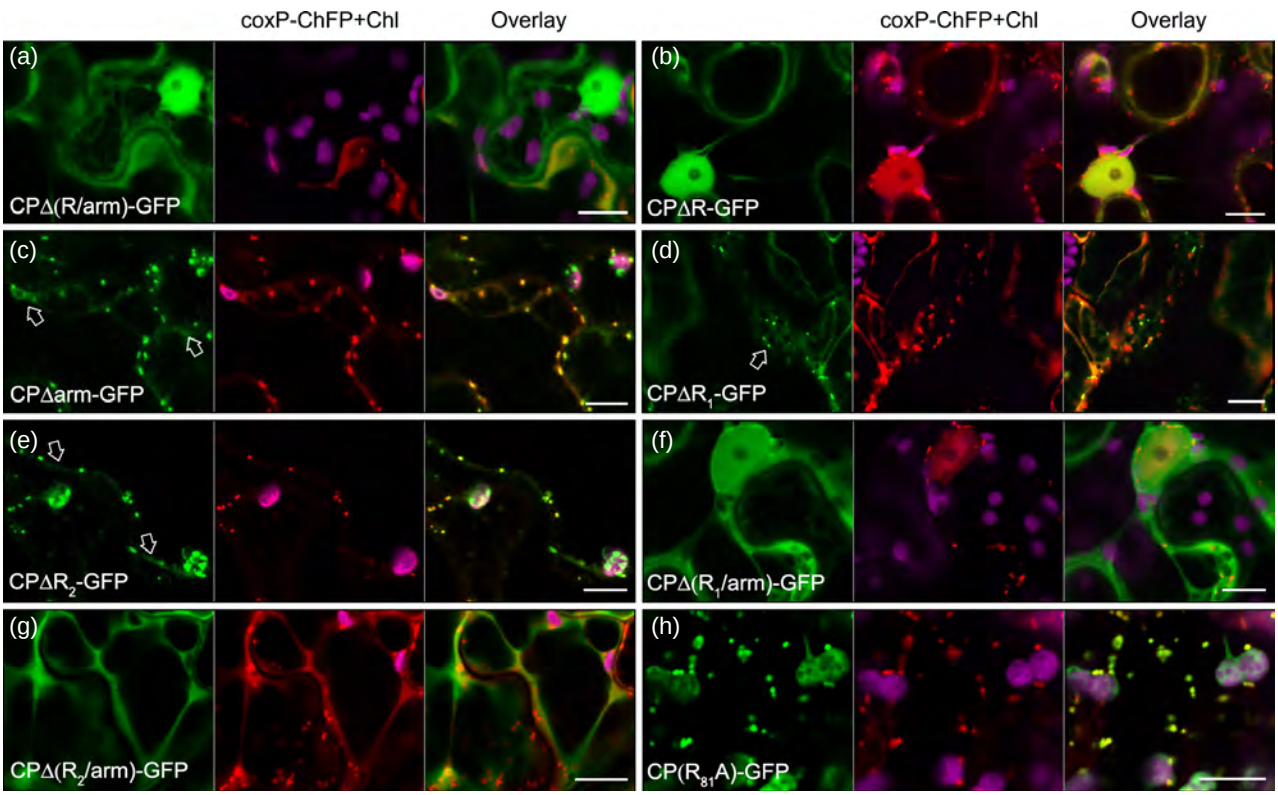

Figure 3. Subcellular localization of C-terminal green fluorescent protein (GFP) fusions of melon necrotic spot virus (MNSV) coat protein (CP) mutants in leaves of *Nicotiana benthamiana* (a-h).
Each panel to the left corresponds to the indicated CP mutant. Panels in the middle are merged images showing coxP-ChFP and chlorophyll (Chl, magenta). Each panel to the right shows the overlay of the above two panels. Arrows in (c) and (e) pointed at cytoplasmic fluorescence, whereas the arrow in (d) pointed to CPΔR_1-GFP spots not colocalizing with mitochondria. Scale bars: 10 μm. Images correspond to single scans.

fluorescence nucleo-cytoplasmic distribution was observed in N-terminal GFP fusions (Figure S6). These results indicated that the R_1 subdomain was essential but not sufficient for an efficient dual organelle import as either the R_2 subdomain or arm region was also required.

Immunoblot analyses showed that the size of nucleocytoplasmic GFP-tagged CPs was as theoretically estimated (Figure S7a). In contrast, the size of CP-GFP, CPΔarm-GFP and CPΔR_2-GFP, which were dually targeted, was smaller than predicted but similar to CPΔ(R/arm)-GFP. Full-length CPΔarm-GFP and CPΔR_2-GFP were slightly detected, most likely associated with the cytoplasmic fluorescence observed in these proteins (Figure S7b). Besides, R/arm-GFP or R/arm/S_{19}-GFP size was similar to GFP (Figure S7c). Together, these results indicate that fusion proteins properly imported to both organelles undergo proteolytic R/arm region cleavage as estimated by size comparison.

MNSV CP has an R_1 subdomain-dependent localization to mitochondria, chloroplasts and mitochondrial-derived VRCs during infection

To rule out the possibility that MNSV CP dual localization could be due to high protein abundance during transient expression from 35Sx2 promoter or different posttranslational mechanisms occurring in healthy versus infected cells, we evaluated CP-GFP localization when expressed under the control of its promoter during infection. To do that, *GFP* was inserted into the MNSV construct behind *CP*, generating pMNSV(CP-GFP). *In vitro* transcripts were inoculated in *N. benthamiana* leaves, and CLSM analysis at 5 days post-inoculation (dpi) revealed small fluorescent infection foci (Figure 4a; Movie S2). Some differences were found between mesophyll and epidermal cells most likely representing early or late stages of infection, respectively. In the former, CP-GFP fluorescence was mainly localized to chloroplast stroma and occasionally in stromules (Figure 4a, inset). The spotted distribution around chloroplast, described above, was rarely observed except in mesophyll cells at the leading edge of the focus, which corresponds to a very early stage of the infection (Figure 4b).

In epidermal cells, CP-GFP fluorescence was also found in chloroplasts, but mainly in small bodies resembling mitochondria and bigger round structures (13.00 ± 3.43 per cell), which were about 3.34 ± 1.20 μm in diameter (Figure 4c). These structures, which were less frequently observed in mesophyll cells (only 2.6 ± 1.3 per cell in 30%

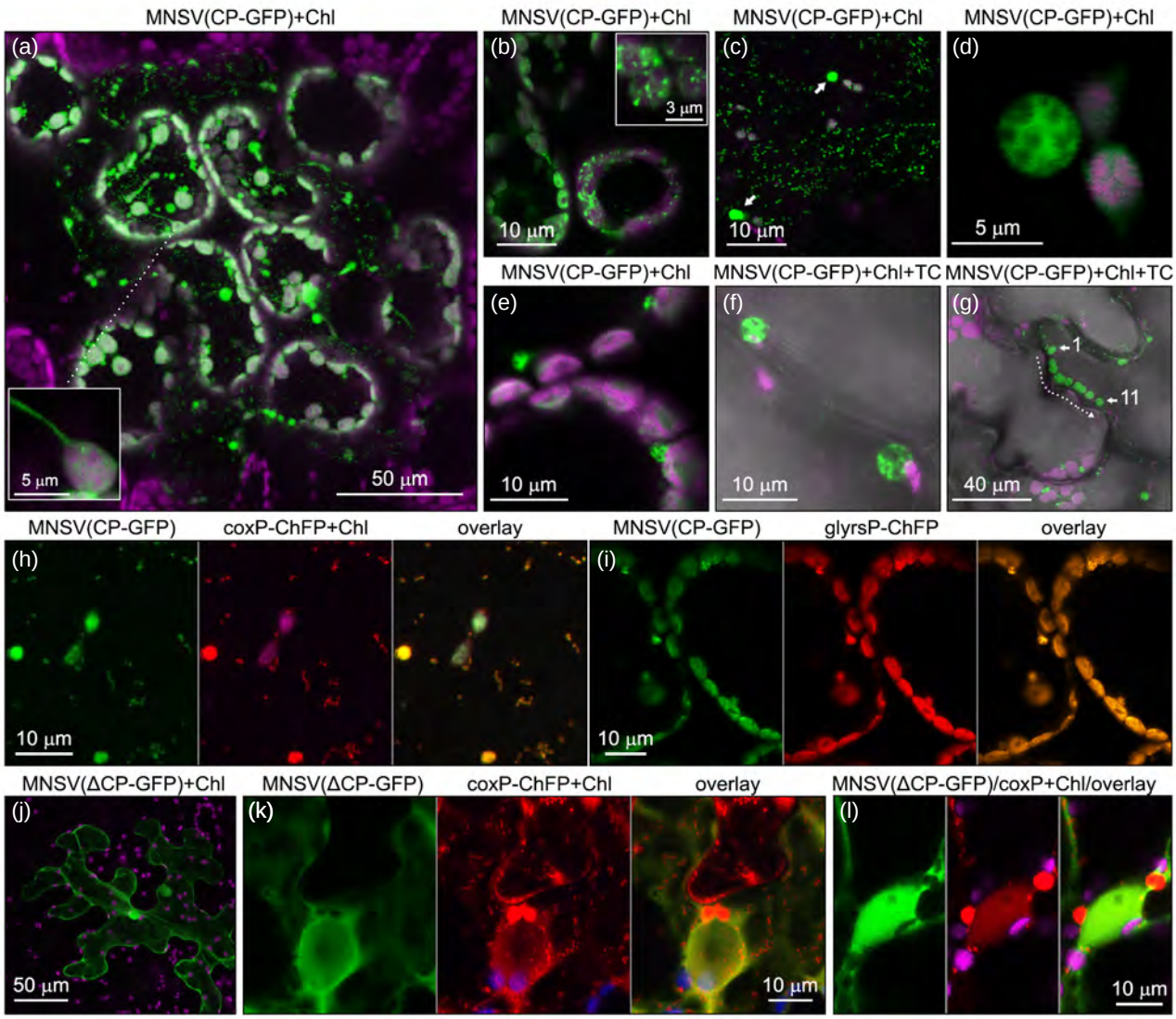

Figure 4. Coat protein (CP)-green fluorescent protein (GFP) subcellular localization during melon necrotic spot virus (MNSV) infection in leaves of *Nicotiana benthamiana* at 5 days post-inoculation (dpi).
(a) Confocal laser-scanning microscopy (CLSM) image showing an MNSV(CP-GFP) infection focus. Inset, single scan showing a chloroplast with CP-GFP in the stroma and extended stromule.
(b) CLSM showing mesophyll cells at the MNSV(CP-GFP) infection focus edge. Inset, chloroplasts with CP-GFP envelope-associated spots.
(c) CLSM image showing CP-GFP fluorescence in chloroplasts, small bodies resembling mitochondria, and round structures (arrows) in epidermal MNSV(CP-GFP) infected cells.
(d) Single scan of a mitochondrial-derived round structure showing uneven fluorescence distribution inside.
(e,f) Single scans of the adjacent region between two mesophyll (e) or epidermal (f) MNSV(CP-GFP) infected cells showing the peripheral localization of mitochondrial-derived round structures.
(g) Stack projection of 11-time series scans (frame time 0.78 sec) showing the displacement of a mitochondrial-derived round structure from positions 1–11.
(h,i) Colocalization of CP-GFP with the mitochondrial marker coxP-ChFP (h) and dual marker glyrsP-ChFP (i) in MNSV(CP-GFP) infected cells.
(j–l) CLSM images showing MNSV(ΔCP-GFP) infected epidermal cells, either alone (in j) or together with the mitochondrial matrix marker coxP-ChFP (in k,l). Chl, chlorophyll in magenta. TC, transmitted channel. CLSM images correspond to Z-stack projections unless indicated.

of analyzed cells), showed an uneven internal distribution of fluorescence, which confers them the appearance of swollen mitochondria with inner vesicles (Figure 4d). The majority were peripherally located in mesophyll and epidermal cells, with some having a certain degree of mobility (Figure 4e,g; Movie S3). Colocalization of small bodies and round structures with coxP-ChFP and glyrsP-ChFP confirmed our assumption about their mitochondrial origin (Figure 4h,i). These swollen mitochondria were similar in form, size, internal organization, intracellular distribution, mitochondrial origin and CP presence to MNSV VRCs previously described in melon (Gomez-Aix et al., 2015), suggesting that they could also constitute viral replication sites. In contrast, inoculation of MNSV(ΔCP-GFP), in which

the CP was replaced by the GFP, resulted in local movement impairment as only single epidermal cells showing nucleo-cytoplasmic fluorescence were observed (Figure 4j). Therefore, CP-GFP must retain some degree of functionality allowing cell-to-cell movement of MNSV(CP-GFP). Altered mitochondria were still observed in MNSV (ΔCP-GFP) infected cells after transient expression of coxP-ChFP (Figure 4k,l).

To determine whether proteolytic processing also occurs during infection, MNSV CP was tagged at the C-terminus with influenza hemagglutinin (HA) epitope into an MNSV infectious construct, generating pMNSV(CP-HA). In addition, HA-tag was also inserted between the arm region and the S domain in pMNSV(C_{HA}P). *In vitro* transcripts of wild-type and both HA-tagged MNSV constructs were inoculated in *N. benthamiana* leaves. The amounts of viral RNAs and HA-tagged CPs were analyzed at different dpi. Regardless of whether the CP was HA-tagged or not, MNSV genomic and subgenomic RNAs were early detected at 2–3 dpi and highly accumulated at 6 dpi (Figure 5a). At 7–8 dpi, similar necrotic lesions were observed in all inoculated leaves (Figure 5b). At 3–4 dpi, CP-HA and C_{HA}P immunodetection resulted in two bands of approximately 35.04 ± 0.24 and 32.07 ± 0.33 kDa (Figure 5c,d, respectively), identical to those observed when CP-HA was produced by agroinfiltration (Figure 5c), and resembling the pattern of the cleaved products reported after immunodetection of CNV CP (Ghoshal et al., 2015). This observation indicates that MNSV CP could be transported to mitochondria and chloroplasts also during infection undergoing N-terminal processing. At 8 dpi, a band of 44.09 ± 0.33 kDa corresponding either to the whole CP-HA or C_{HA}P (theoretical size: 43.03 kDa) was detected. However, the intensities of bands corresponding to the cleaved CP were always higher than that of the complete ones. These results contrast with what was found in CNV infection, where only 1–5% of the CP was reported to target chloroplasts and mitochondria (Xiang et al., 2006).

Considering the estimated size of the bands and the results previously published about CNV CP, three MNSV CP-HA deletion proteins starting at position 65 (CPΔ_{2-64}-HA), 81 (CPΔ_{2-80}-HA), and 96 (CPΔ_{2-95}-HA) were designed (Figure 5e). After agroinfiltration, the three proteins were analyzed by Western blot, and their migration was compared with CP-HA (Figure 5f). The upper and lower cleavage products obtained from both MNSV(CP-HA) infection or CP-HA agroinfiltration co-migrated with CPΔ_{2-80}-HA and CPΔ_{2-95}-HA, indicating that CP processing in mitochondria and chloroplasts may occur at two different but close points, one of them within the arm region but near the arm/S domain junction where most likely the second one occurs, as previously described for CNV CP (Ghoshal et al., 2015).

To further evaluate whether R/arm-GFP expression during infection also acts as a cytopathogenic elicitor, we generated pMNSV(R/arm-GFP) by deleting both S and P domains in pMNSV(CP-GFP). Although very small multicellular foci were occasionally observed (Figure 6a), the infection was mainly restricted to single cells at 5 dpi (Figure 6b). R/arm-GFP localization in multicellular foci was similar to that described above for CP-GFP in MNSV(CP-GFP), except that VRCs were more frequently detected. Approximately 70% of mesophyll cells displayed numerous VRCs ubiquitously distributed throughout the cell (Figure 6a, inset). VRC number per mesophyll cell was also significantly higher than that observed in MNSV(CP-GFP) foci (12.36 ± 7.87, $t = 4$ and $P = 0.0021$), although no difference was observed between epidermal cells (12.83 ± 4.07, $t = 0.086$ and $P = 0.9$). In contrast, no fluorescence-labeled VRCs were detected in unicellular foci. Instead, most chloroplasts extended stromules to and contacted the nucleus forming perinuclear clusters as occurred upon transient R/arm-GFP expression (Figure 6b–d). Moreover, colocalization with coxP-ChFP revealed that mitochondria in these unicellular foci mainly showed an abnormal ring-shaped morphology similar to spheroids and annular mitochondria observed in animal cells and Arabidopsis protoplasts, respectively, before stress-induced cell death (Miyazono et al., 2018; Scott and Logan, 2008; Figure 6e,f).

To study the relevance of the R_1 subdomain in CP import during infection, an additional construct, pMNSV(CP$\Delta R_{1[6-30]}$-GFP), containing a deletion of the aa positions 6–30, was made. Due to overlapping between contiguous p7B and CP open reading frames (ORF), the first five aa positions (MAMVR) of the R_1 subdomain remained. After 4–5 dpi, only small multicellular foci were detected, showing CP$\Delta R_{1[6-30]}$-GFP fluorescence in the cytoplasm but not in the nucleus of both mesophyll and epidermal cells (Figure 6g; Movie S4). Some cells also showed small bodies that did not colocalize with dual marker glyrsP-ChFP (Figure 6h). Expression of coxP-ChFP also confirmed the presence of VRCs in infected mesophyll cells, but they were found in groups or even forming a single large cluster consisting of more than 15 units (Figure 6i). This situation contrasts with that observed in mesophyll cells infected with MNSV(CP-GFP) or MNSV(R/arm-GFP), suggesting that although CP is not necessary for VRC formation, it could modulate their biogenesis and dynamic behavior.

MNSV p29 auxiliary replicase was localized at the boundaries of swollen mitochondria that form ER-associated small clusters and large juxtanuclear aggregates

To further evaluate the contribution of p29 in mitochondrial modification, VRC formation and its relationship with CP, we ectopically expressed a fluorescent-tagged p29 either alone or in combination with a mitochondrial matrix marker or CP. When p29 was expressed alone, the most striking observation, not described previously, was the appearance

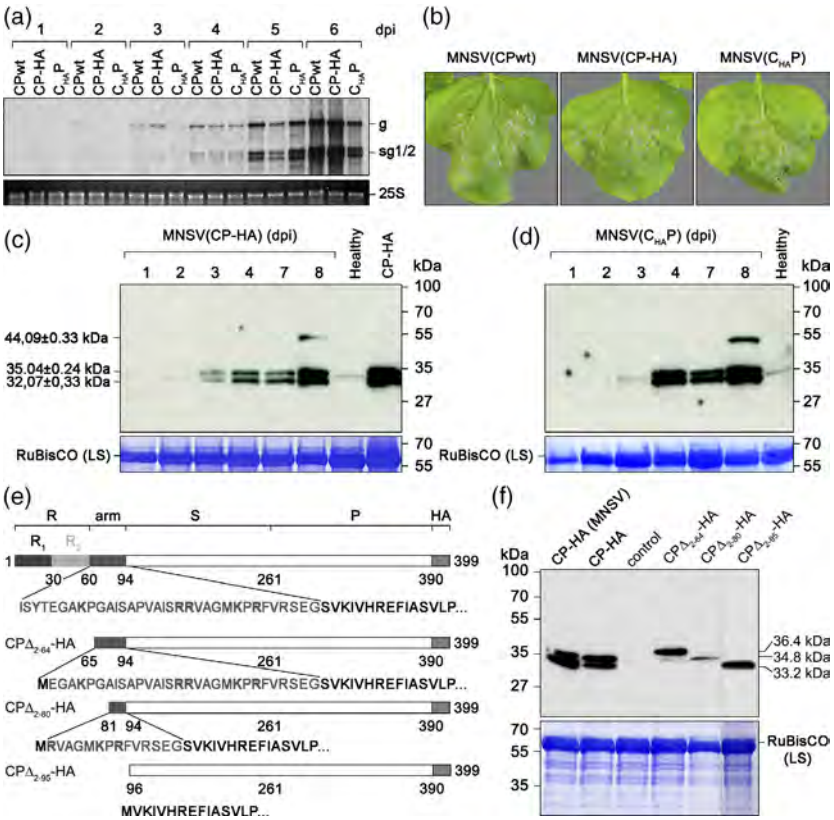

Figure 5. Coat protein (CP)-hemagglutinin (HA) undergoes cleavage at two different points during both infection and agroinfiltration.
(a) Northern blot analysis of melon necrotic spot virus (MNSV) RNAs at the indicated days post-inoculation (dpi). The position of genomic and both subgenomic RNAs is indicated. Ethidium staining of ribosomal RNA 25S is shown as loading control.
(b) Images of *Nicotiana benthamiana* leaves inoculated with the indicated viral RNAs taken at 8 dpi.
(c,d) Immunodetection of CP-HA and $C_{HA}P$ expressed from MNSV genome during local infection of *N. benthamiana* at the indicated dpi [MNSV(CP-HA)]. The last track in (c) corresponds to CP-HA obtained 48 h after agroinfiltration of a binary plasmid in *N. benthamiana*. Leaves from three plants were analyzed at each time point and mixed in one sample. The molecular weight of the resulting bands was estimated by linear regression and indicated.
(e) Schematic representation of the MNSV CP domains (R, arm, S, and P plus the HA tag) and the three CP-HA deletion proteins starting at position 65 ($CP\Delta_{2-64}$-HA), 81 ($CP\Delta_{2-80}$-HA) and 96 ($CP\Delta_{2-95}$-HA).
(f) Size comparison of the two CP-HA cleavage products obtained either from MNSV infection or agroinfiltration with $CP\Delta_{2-64}$-HA, $CP\Delta_{2-80}$-HA and $CP\Delta_{2-95}$-HA by Western blot. The size of $CP\Delta_{2-64}$-HA, $CP\Delta_{2-80}$-HA and $CP\Delta_{2-95}$-HA is indicated on the right. Coomassie blue stainings are shown as loading controls. The positions of the protein molecular weight markers with sizes in kDa are indicated.

of a large round-shaped structure (11.95 ± 2.22 μm in long axis) near the nucleus, together with free and vesicle-associated punctate bodies over the cytoplasm in epidermal cells (Figure 7a,b) or peripherally located in mesophyll cells (Figure 7c). Single scan analysis along the Z-axis revealed that juxtanuclear structures consisted of a large cluster of size-heterogeneous vesicles showing uneven p29-GFP accumulation around them (Figure 7a, inset; Movie S5). Interestingly, large clusters and cytoplasmic bodies/vesicles were found in association with the ER (Figure 7d). To assess the nature of these structures, the mitochondrial matrix marker coxP-ChFP and p29-GFP were co-expressed. In a general view, both proteins appeared to overlap partially (Figure 7e, f), but magnification images revealed that coxP-ChFP was actually in close association with the p29-labeled cytoplasmic bodies or inside vesicles (Figure 7g,h). Accordingly, coxP-ChFP and p29-GFP aggregated together in juxtanuclear structures as before (12.14 ± 1.67 μm in long axis, $t = 0.33$ and $P = 0.73$), but their distribution profiles were opposite to each other, suggesting different localization. p29 could be associated with membranes of altered mitochondria, as reported previously, and coxP-ChFP in the matrix (Figure 7i–k). On the other hand, upon co-expression with p29-ChFP, CP-GFP fluorescence was observed inside p29-GFP-labeled vesicles in smaller juxtanuclear structures (9.87 ± 2.34 μm in long axis, $t = 3.4$ and $P = 0.0015$; Figure 7l,m), indicating that CP-GFP behaved as a mitochondrial matrix protein.

MNSV CP import into mitochondria and chloroplasts could prevent p29-induced necrosis, but compromises RSS and encapsidation capacities

Mochizuki et al. (2009) showed that p29 expressed from a CMV-based vector modifies mitochondrial membrane

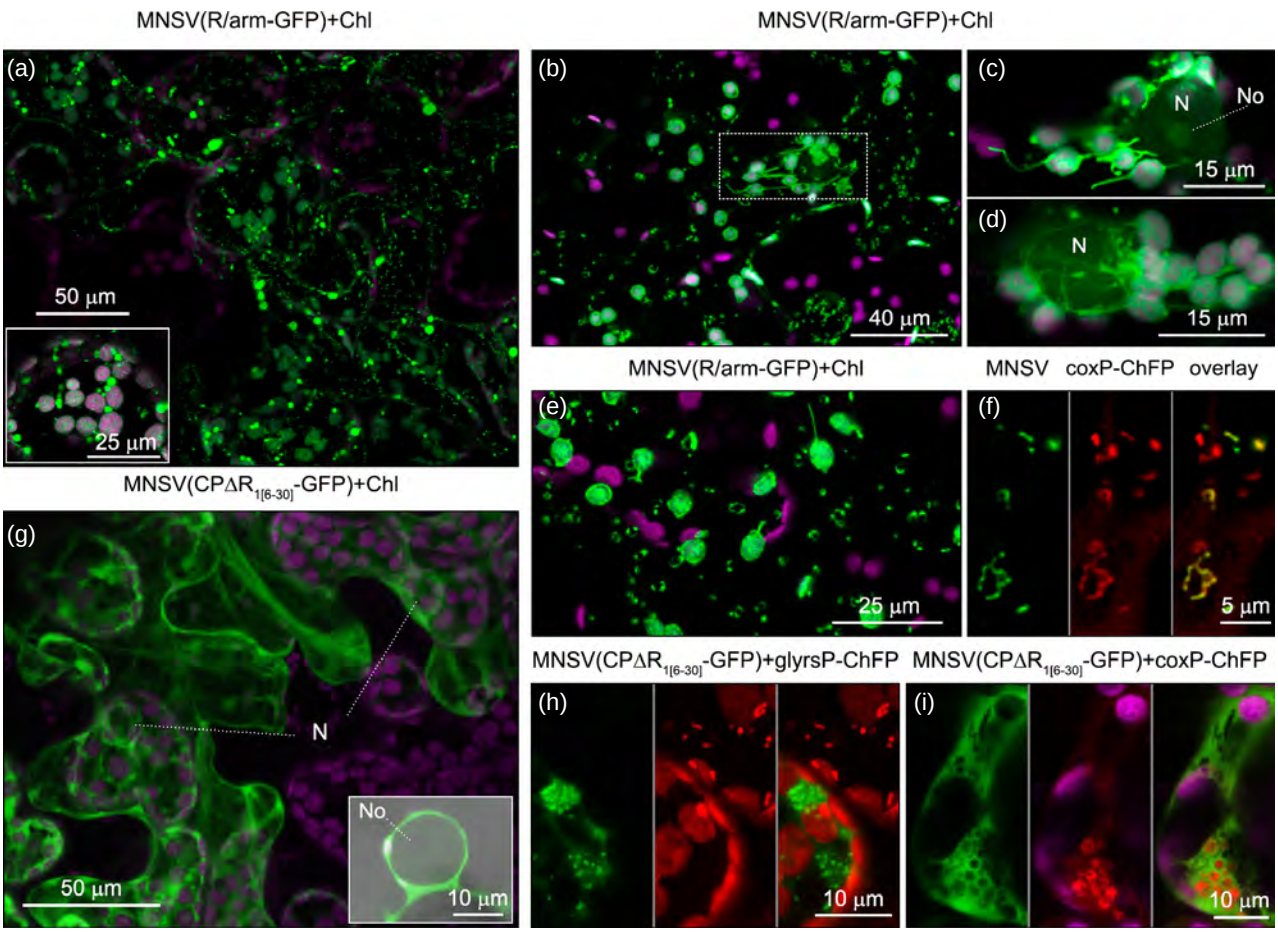

Figure 6. Subcellular localization of R/arm-green fluorescent protein (GFP) and CPΔR$_{1[6-30]}$-GFP during melon necrotic spot virus (MNSV) infection in leaves of *Nicotiana benthamiana* at 5 days post-inoculation (dpi).

(a) Confocal laser-scanning microscopy (CLSM) image of a local MNSV(R/arm-GFP) infection foci. R/arm-GFP fluorescence was found in chloroplasts, normal and swollen mitochondria (VSM). Inset shows an infected mesophyll cell.

(b) CLSM image of an isolated single cell infected by MNSV(R/arm-GFP). Single scan magnification of the dotted rectangle is shown in (c). A detailed view of a juxtanuclear cluster of chloroplasts and cytoplasm with ring-shaped mitochondria are shown in (d) and (e), respectively.

(f) Single scan images showing colocalization of ring-shaped mitochondria with coxP-ChFP.

(g) CLSM image of a local MNSV(CPΔR$_{1[6-30]}$-GFP) infection foci. Inset shows CPΔR$_{1[6-30]}$-GFP fluorescence in the cytoplasm around the nucleus merged with the transmitted channel.

(h) CLSM images of two adjacent mesophyll cells showing the different distribution of mitochondria (coxP-ChFP) between the MNSV(CPΔR$_{1[6-30]}$-GFP) infected cell on the left, and the healthy one on the right.

(i) Single scan of an MNSV(CPΔR$_{1[6-30]}$-GFP) infected mesophyll cell showing a large and single cluster of mitochondrial-derived round structures labeled with coxP-ChFP. Chl, chlorophyll in magenta. TC, transmitted channel. CLSM images correspond to Z-stack projections unless indicated.

structures generating mitochondrial damage and necrosis in *N. benthamiana*. Accordingly, we have shown that p29 transient expression induced mitochondrial swelling and juxtanuclear aggregation, but also triggered necrosis in localized areas at 5–6 dpi in single expression or together with GFP, CPΔ(R/arm)-GFP and R/arm-GFP (Figure 8a). Necrosis was most prominent and affected the whole leaf when p29 was co-expressed either with the silencing suppressor HCPro of tobacco etch virus or CPΔR$_1$-GFP. Instead, p29-HA co-expression with CP-GFP either abolished (left side of the panel) or considerably reduced (right side of the panel) necrosis appearance. Western blot analysis performed at 1, 2, 3 and 4 dpi, before necrosis appearance, showed that the levels of p29-HA in the presence of GFP, CPΔ(R/arm)-GFP, R/arm-GFP or CP-GFP were not significantly different from each other ($F = 3.82$, $P = 0.058$), but all of them were significantly lower than those found in HCPro and CPΔR1-GFP co-expressions ($F = 75$, $P < 0.0001$, calculated at 2 dpi, and adjusted P-values for multiple comparisons with CP are shown in Figure 8b). Northern blot analysis at 2 dpi was consistent with Western blot results as p29-HA mRNA accumulated more in the presence of HCPro, which showed the highest levels, or CPΔR1-GFP, than CP and the rest of the proteins (Figure 8c). Therefore, the higher p29 levels the greater is necrosis but, at equal amounts, only the complete CP

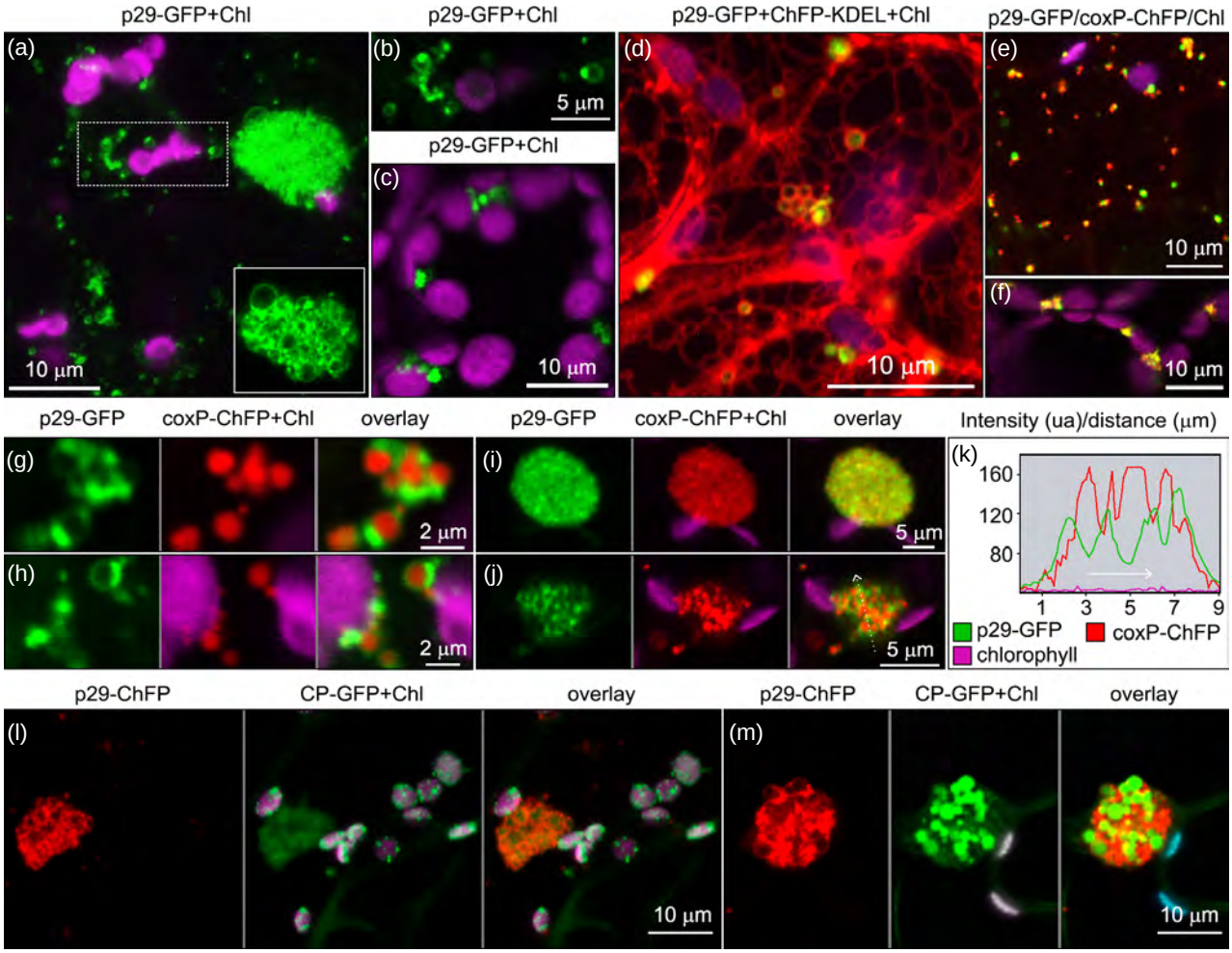

Figure 7. Transient expression of p29 auxiliary replicase can induce mitochondrial swelling and aggregation in leaves of *Nicotiana benthamiana*.
(a) p29 subcellular localization in epidermal cells. A juxtanuclear structure single scan is shown on the bottom inset.
(b) Single scan magnification of the dotted rectangle in (a).
(c) Single scan showing p29-green fluorescent protein (GFP) bodies and vesicles peripherally located in mesophyll cells.
(d) p29-GFP localization in the nuclear envelope, endoplasmic reticulum (ER) and ER-associated bodies.
(e,f) Co-expression of p29-GFP and coxP-ChFP in epidermal (e) and mesophyll (f) cells.
(g,h) Single scans showing p29-labeled cytoplasmic vesicles containing coxP-ChFP.
(i) coxP-ChFP localization in a large oval-shape aggregate upon co-expression with p29-GFP.
(j) Single scan showing the differential distribution of coxP-ChFP and p29-GFP in large aggregates.
(k) Fluorescence intensity profile of indicated fluorophores plotted versus distance along the arrow in (j).
(l) Confocal laser-scanning microscopy (CLSM) image showing coat protein (CP)-GFP localization in a large aggregate near the nucleus upon co-expression with p29-ChFP.
(m) Single scan showing an aggregate of p29-ChFP-labeled vesicles showing CP-GFP fluorescence inside.

attenuated necrosis. In previous work, using 16c GFP-transgenic plant system, we showed that siRNA binding through the R_2/arm region confers to CP and CPΔR_1, RSS activity at systemic, but not local, level (Serra-Soriano et al., 2017). The results presented here suggest that CPΔR_1 acts as a strong local suppressor favoring p29 expression but, in contrast to HCPro, this effect was only noticeable earlier after CPΔR_1 expression. This could be the reason for negative results in the 16c system as samples were analyzed at 5 dpi. To clarify this issue, we used a new approach based on an alfalfa mosaic virus (AMV) RNA 3 expression vector and transgenic *Nicotiana tabacum* plants that express the P1 and P2 subunits of the AMV replicase (P12 plants; Martínez-Pérez et al., 2019). This method is a fast and reliable technique based on the correlation between symptomatology on inoculated leaves and suppressor activity. According to reported data, inoculation of P12 leaves with AMV RNA 3 expressing CP or GFP did not produce local symptoms. In contrast, AMV RNA 3 expressing CPΔR_1 generated extended necrotic lesions (Figure 8d). These data together indicate that CPΔR_1 is more efficient than CP as a suppressor at local level. Nevertheless, to

further investigate this notion, we introduced CP$\Delta R_{1[6–30]}$-HA into the construct pMNSV(CP$\Delta R_{1[6–30]}$-HA), and the corresponding transcripts were inoculated in *N. benthamiana*. Viral RNA and CP$\Delta R_{1[6–30]}$-HA accumulation in infected leaves were compared with those obtained with the wild-type variant at 8 dpi (Figure 8e). Depending on the sample, MNSV(CP$\Delta R_{1[6–30]}$-HA) RNA levels were lower than or similar to wild-type, but the levels of the single uncleaved CP$\Delta R_{1[6–30]}$-HA band, which was detected, were consistently higher than those of the two cleaved CP-HA products obtained in wild-type infection. Therefore, the potential of CP to suppress RNA silencing is compromised by its organelle targeting that implies its cytoplasmic depletion and its R/arm domain processing, a region essential for its role as RSS (Serra-Soriano et al., 2017).

Considering that the R_2/arm domain is also required for MNSV genome encapsidation (Serra-Soriano et al., 2017), virus assembly could also be affected by CP processing upon organelle import. To examine this view, virions were isolated from photosynthetic (leaves and stems/petioles) and non-photosynthetic (roots) infected tissues. The process was repeated three times (two replicates are shown in Figure 9a), and consistently showed that virions accumulated in inverse proportion to the photosynthetic capacity of the tissue, higher in roots (10–20 times) and stems/petioles (5–10 times) than in leaves, where they were barely detected. To analyze whether the differential accumulation of virions could be related to different processing levels of the CP, we express CP-HA in *N. benthamiana* plants using a tobacco rattle virus (TRV)-based binary vector, $TRV2_{promPEBV}$[CP-HA] (MacFarlane and Popovich, 2000). This heterologous expression system ensures that transit peptide is not precluded by virion assembly and only uncoated CP is detected. A TRV vector expressing ChFP was generated, $TRV2_{promPEBV}$[ChFP], to visualize the virus spreading through the plant. One week after inoculation of *N. benthamiana*, $TRV2_{promPEBV}$[ChFP] fluorescence was observed in upper leaves, stems and roots (Figure 9b). At this time, proteins from three $TRV2_{promPEBV}$[CP-HA] infected plants were extracted and analyzed by Western blot. According to that observed above during MNSV infection (Figure 4b), two CP-HA cleavage products of approximately the same size as before were detected (protein sizes calculated by regression analysis of electrophoretic mobility are shown in Figure 9c). Consistent with the tissue-specific accumulation of virions, full-length CP-HA (theoretical size 43.03 kDa) was detected in all root samples and, at least, in stem replicate two.

In contrast, no full-length CP was observed in leaves. In any case, a high proportion of processed CP was still observed in all tissues. To explain this, we analyzed CP subcellular localization in stems and roots with an additional TRV vector expressing R/arm-GFP, $TRV2_{promPEBV}$[R/arm-GFP]. One week after inoculation, $TRV2_{promPEBV}$[R/arm-GFP] fluorescence was observed in mitochondria and chloroplasts of upper leaves and stems (Figure 9d). In roots, R/arm-GFP-labeled non-photosynthetic plastids, as chlorophyll fluorescence was not detected, mainly clustered around the nucleus and showing long stromules. This targeting of the R/arm-GFP to non-photosynthetic plastids could explain the high degree of CP-HA processing still observed in this tissue. Moreover, fluorescent mitochondria were also detected in roots but, compared with green tissues, considerably fewer of them were observed.

Effect of R/arm CP mutations on MNSV infectivity and HR-related gene expression

To explore how CP mutations affected MNSV infection in *N. benthamiana*, 2-week-old seedlings were inoculated with *in vitro* transcripts of MNSV and all N-terminal deletion mutants used in this study as well as $R_{81}A$ point mutant. Five days later, leaves inoculated with MNSV-CPΔR_1 or MNSV-CP($R_{81}A$) showed necrotic or chlorotic symptoms, respectively, whereas the rest of the mutants caused no local symptoms. MNSV-CPΔ(R/arm) was taken as representative of symptomless variants for further analysis (Figure S8). Necrotic lesions generated by MNSV-CPΔR_1 were significantly smaller than those observed in wild-type MNSV infections (0.78 ± 0.47 versus 2.17 ± 1.07 mm^2, $t = 5.8$, $P < 0.0001$). At 15 dpi, necrosis nearly or fully covered MNSV inoculated leaves whereas, in MNSV-CPΔR_1, local symptoms still consisted of well-defined necrotic lesions (3.73 ± 1.35 mm^2; Figure S8). Only 2 out of 30 (6.7%) plants inoculated with MNSV-CPΔR_1, versus 27 out of 30 (90%) of those inoculated with MNSV, showed systemic symptoms (Figure S8). Those consisted of necrosis associated with local lesions, chlorotic in the beginning, stems and interveinal tissue of upper leaves, leaf malformation, dwarfing and occasionally plant death (Figure S8). All plants inoculated with MNSV-CP($R_{81}A$) and the rest of the mutants remained symptomless at the systemic level. MNSV systemic infection was confirmed by dot-blot hybridization analysis (Figure S8).

Samples from inoculated leaves were collected at 5 dpi and total RNA extracted. Although CPΔR_1 could enhance early viral replication compared with CP($R_{81}A$), the Northern blot analysis revealed that MNSV-CPΔR_1 and MNSV-CP ($R_{81}A$) RNAs accumulated similar to each other ($q = 1.9$, $P = 0.58$), although significantly lower than wild-type viral RNAs ($q = 7.6$, $P = 0.003$; $q = 9.5$, $P = 0.0007$, respectively). In contrast, RNAs from MNSV-CPΔ(R/arm), which was selected as representative of symptomless mutants, were barely detected compared with wild-type viral RNAs ($q = 17.5$, $P < 0.0001$; Figure 10a). All events described here, including mitochondrial swelling and aggregation, stromules induction, as well as necrosis and systemic resistance, are consistent with a HR (Mur et al., 2007; Scott and Logan, 2008). To impede pathogen spreading, HR causes

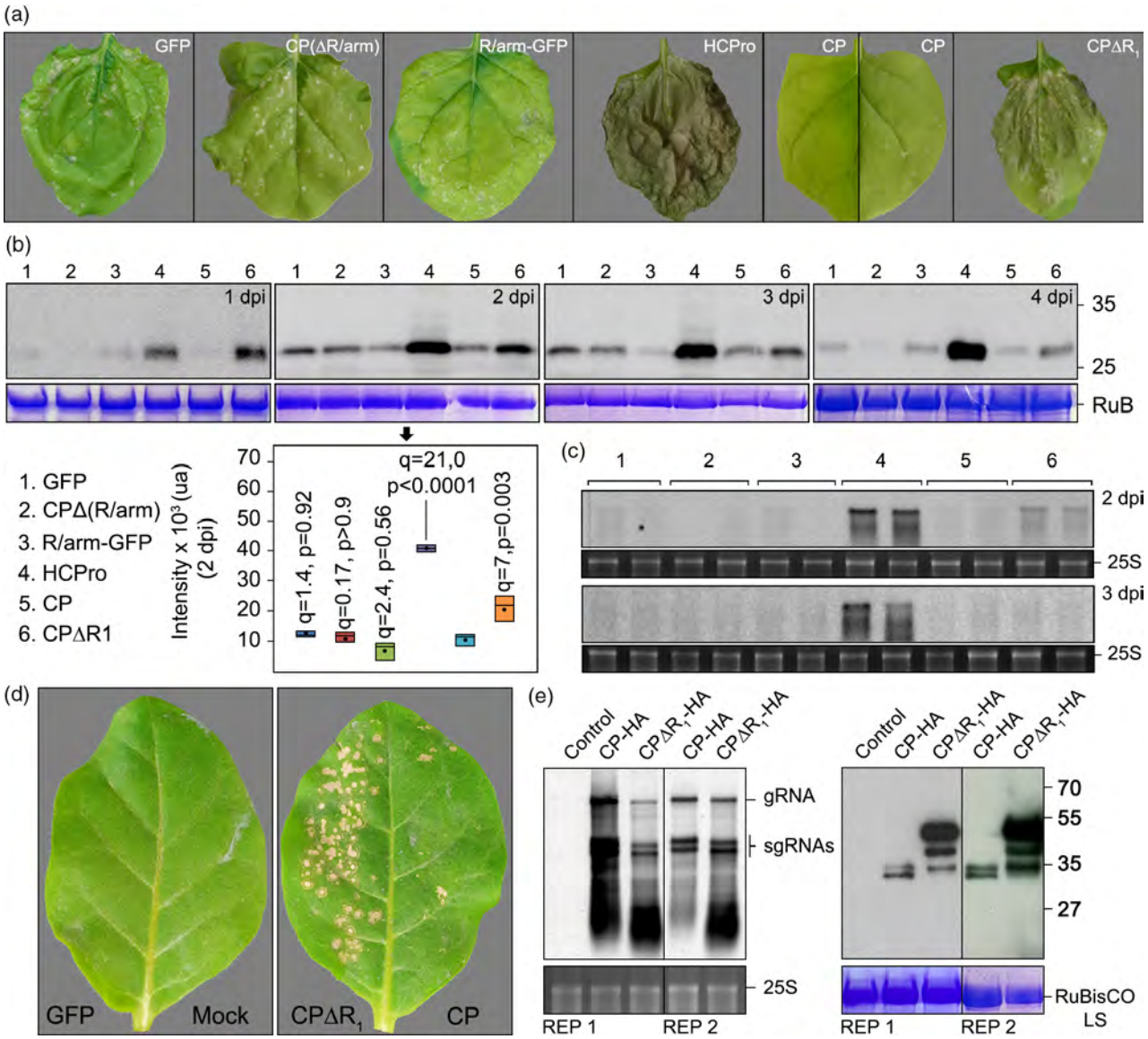

Figure 8. Coat protein (CP)-green fluorescent protein (GFP) inhibition of p29-hemagglutinin (HA) induced necrosis in transient expression assays and analysis of RNA silencing suppressor (RSS) capacity of melon necrotic spot virus (MNSV) CPΔR_1.

(a) Effect of GFP, CPΔ(R/arm)-GFP, R/arm-GFP, CPΔR_1, CP or TEV HCPro on p29-HA induced necrosis upon co-expression in leaves of *Nicotiana benthamiana*. Images were taken at 6 days post-inoculation (dpi).

(b) Representative Western blot analysis to detect p29-HA in protein extracts from *N. benthamiana* leaves co-expressing the indicated proteins at 1, 2, 3 and 4 dpi. Boxplot represents the chemiluminescence intensity of p29-HA band from three independent replicates at 2 dpi. The lower and upper limits of the boxes are plotting the min and max values, respectively, whereas the lines dividing them represent the median values. Points inside boxes represent the mean from the three replicates. $P < 0.05$ indicates statistical significance. Coomassie blue staining of RuBisCO is shown as loading control.

(c) Northern blot analysis from two independent replicates to detect p29-HA mRNA. RNAs were extracted from leaves co-expressing the indicated proteins at 2 and 3 dpi. Ethidium bromide staining of 25S ribosomal RNA is shown as loading control.

(d) Comparison of the silencing suppressor activity of CP and CPΔR1, using AMV RNA 3 expression vector and transgenic P12 plants of *Nicotiana tabacum*. AMV RNA 3 transcripts expressing GFP, CP or CPΔR_1 were inoculated on different leaf halves as indicated.

(e) Analysis of the accumulation of viral RNAs and CP in MNSV(CPΔ$R_{1[6-30]}$-HA) and MNSV(CP-HA) by Northern blot (left) and Western blot (right), respectively. Three replicates were performed consisting of a tissue mix from three plants. Two of them are shown.

the rapid death of cells at the initial point of infection concurrent with the production of ROS and defense gene upregulation (Heath, 2000). Therefore, we examined the RNA expression of *ZAT10*, a regulatory transcription factor for oxidative stress signaling (Fujita et al., 2009), *APX2*, an antioxidant cytosolic ascorbate peroxidase (Caverzan et al., 2012), HR markers *HIN1* (Gopalan et al., 1996) and *HSR203J* (Pontier et al., 1998), and pathogenesis-related *PR1* (van Loon, 1997) genes by quantitative real-time reverse transcription polymerase chain reaction (qRT-PCR) shown in

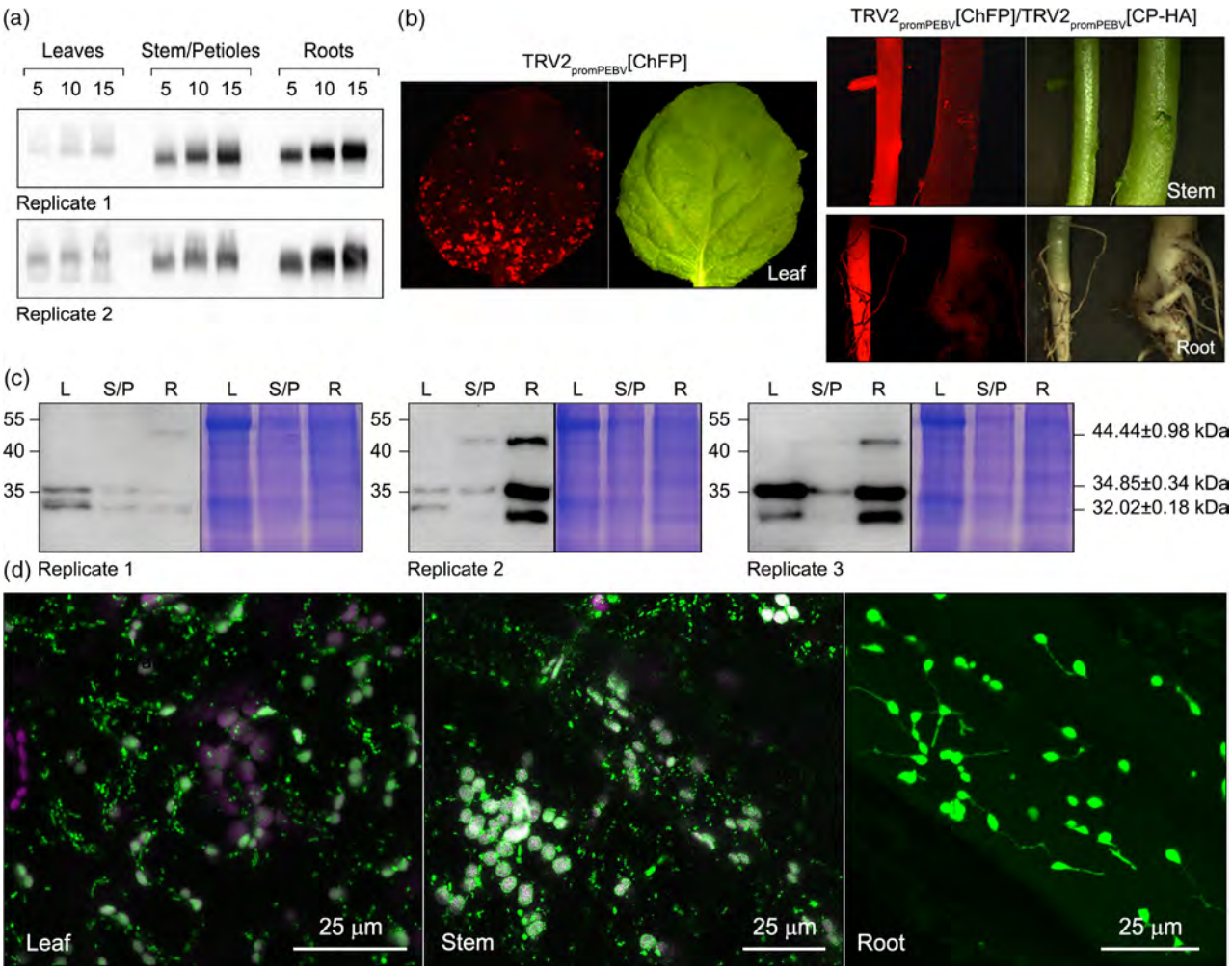

Figure 9. Melon necrotic spot virus (MNSV) virion accumulation, coat protein (CP)-hemagglutinin (HA) processing, and R/arm-green fluorescent protein (GFP) subcellular localization in leaves, stems and roots.

(a) Northern blot analysis of MNSV virions isolated from roots, stems, and petioles and leaves of MNSV-infected *Nicotiana benthamiana* plants in two independent replicates. Equal extract volumes (5, 10 and 15) from the same fresh weight of each tissue were loaded.

(b) Images of leaves, stems and roots of *N. benthamiana* plants infected with $TRV_{promPEBV}$[ChFP] or $TRV_{promPEBV}$[CP-HA] taken under white or ultraviolet/rhodamine filter light 1 week after inoculation.

(c) Western blot analysis to detect CP-HA expressed from a tobravirus-based vector in roots (R), stems and petioles (S/P), and leaves (L) of *N. benthamiana*. Results from three different plants are shown. Coomassie blue staining is shown as loading control. Protein sizes calculated by regression analysis of electrophoretic mobility are shown on the right. The positions of the protein molecular weight markers with sizes in kDa are indicated on the left.

(d) Confocal images of cells from leaves, stems and roots of *N. benthamiana* plants infected with TRV1 plus $TRV2_{promPEBV}$[R/arm-GFP] 1 week after inoculation.

Figure 10(b). PCR results indicated that, except for *APX2*, all markers were induced in MNSV and MNSV-CPΔR_1 infections in the same order of magnitude (Figure 10b). *HIN1* and *PR1* were strongly upregulated to levels similar to those seen in homologous *HIN1* (Li et al., 2012) and other members of the PR family (Fister et al., 2016) under biotic stress. In comparison to *HIN1*, a lower induction was observed for the second HR marker *HSR203J* (four–five-fold). Nevertheless, it has been described that *HSR203J* and *HIN1* are induced approximately at the same order of magnitude early upon pathogen attack but, when necrosis appeared, *HIN1* upregulation further increased while *HSR203J* induction fell to $1/10^{th}$ of *HIN1* (Li et al., 2012). Considering that MNSV-infected samples were taken at 5 dpi when necrosis was macroscopically visible, *HSR203J* mRNA levels might be within the expected values. Concerning *ZAT10*, it was 14- and 11-fold induced in MNSV and MNSV-CPΔR_1 infections, respectively. These values are similar to those reported for abiotic (Rossel et al., 2007) and biotic stresses, such as those induced by the necrotrophic fungus *Botrytis cinerea* in Arabidopsis (AbuQamar et al., 2006). Compared with previous data, PR1 was barely induced (sixfold) in non-necrotic MNSV-CP(R_{81}A) and MNSV-CPΔ(R/arm) infection, whereas the rest of the

markers were not significantly induced. *APX2* was not significantly upregulated in any case ($F = 2.17$, $P = 0.15$).

DISCUSSION

Dual targeting is emerging as an evolutionary solution for some plant pathogens, constrained by small genomes, to expand and diversify protein function. However, only a few examples of dual targeting to mitochondria and chloroplasts, mainly including some fungus effectors and CNV CP, have been described (Hui et al., 2010; Liu et al., 2018; Petre et al., 2015). Here we show that MNSV CP is also dually targeted to these organelles during ectopic expression, as well as to mitochondrial-derived VRCs in infected cells, and unravel the implications that this ambiguous targeting has on the viral infection cycle. Prediction analysis revealed that mitochondrial and/or chloroplast targeting could be extended among tombusvirus CPs, indicating that MNSV CP similarity is beyond structural features. Sequences in the R/arm domain were required in MNSV and CNV CP import, but we found some differences in dTP structural organization. Mitochondrial and chloroplast targeting information rely on distinct regions in CNV dTP (Hui et al., 2010), whereas MNSV dTP seems to contain a unique ambiguous signal. It is known that sorting information is mainly localized within the 19 N-terminal amino acids of transit peptides. Accordingly, the R_1 subdomain showed similar mTP and cTP traits except for the presence of polar asparagine instead of serine (Berglund et al., 2009; Ge et al., 2014). This bias towards nitrogenous asparagine was observed in the apicoplast transit peptide of the malaria parasite *Plasmodium falciparum*, which was hypothesized to be caused by differences in codon usage and nitrogen disposal (Ralph et al., 2004). R_1 subdomain was shown to be essential but not sufficient for CP organelle import as, regardless of their primary structure, either R_2 subdomain or arm regions were also required. As previously described for some Arabidopsis proteins, a 60-aa minimum length could be necessary as it was proposed that a longer than 20-aa spacer between cTP and mature protein relieves steric hindrance, enabling the binding of essential translocators (Berglund et al., 2009; Shen et al., 2017). Therefore, R_2/arm regions, which are relevant RNA binding domains (Serra-Soriano et al., 2017), are acting here as a mere spacer between R_1 and the folded S domain.

Developmental and physiological states of mitochondria and chloroplasts play a role in sensing environmental conditions and eliciting adaptive plant responses. In this process, coordinated organelle-to-nucleus retrograde signaling, which results in nuclear expression changes and, occasionally, cell death, is essential (Reape et al., 2015; Wang et al., 2020). Also, mitochondria and chloroplasts have been revealed as critical organelles in regulating plant–virus interactions (Li et al., 2016; Zhao et al., 2016). Mitochondria and chloroplasts can coordinate plant defense response and cell death through shared retrograde signaling pathway components, some of them targeting both organelles (Wang et al., 2020; Yang et al., 2021). Moreover, several key antioxidative enzymes in the ascorbate-glutathione cycle and mitochondrial anti-apoptotic proteins from animals are also dually targeted to mitochondria and chloroplasts in plants. ACD2, which protects against cell death caused by *Pseudomonas syringae*, was localized in both organelles in Arabidopsis young seedlings but only in chloroplasts in mature leaves. Interestingly, MNSV CP was rarely immunolocalized in chloroplasts of melon cotyledons, suggesting that dual localization could be host- or tissue-dependent (Gomez-Aix et al., 2015; Miras et al., 2020). In any case, the same authors reported that the expression of many chloroplast and photosynthesis-related genes was inhibited during MNSV infection of melon cotyledons (Gómez-Aix et al., 2016). Mitochondria and chloroplasts are thus valuable targets for plant pathogenic effectors to efficiently interfere with retrograde signaling and control immune response (Liu et al., 2018; Petre et al., 2015).

Two MNSV components produced HR-compatible cytopathic effects on mitochondria and/or chloroplasts, uncovering their role in plant perception of the pathogen. On the one hand, the R/arm domain induced chloroplast clustering around the nucleus and communication among them through stromule extension (see a summary of the functions of the different domains of MNSV CP in Table S1). Degradation of signal peptides generated in mitochondria and chloroplasts is essential for proper plant development (Kmiec et al., 2014). Therefore, after viral CP processing inside the organelles, peptide accumulation derived from the R/arm domain could exceed the capacities of the organellar oligopeptidases to degrade them. This situation could be perceived by chloroplasts and mitochondria as a stress signal triggering their movement to and communication with the nucleus. It has been reported that this is a general response to pathogen challenge during pattern-triggered immunity and ETI, allowing pro-defense signals, such as ROS and NRIP1, to travel into the nucleus triggering cell death. This was evidenced by enhanced HR-like cell death response to *P. syringae* in Arabidopsis knockouts constitutively expressing stromules (Caplan et al., 2015; Ding et al., 2019).

On the other hand, the interaction of p29 with the mitochondrial membrane induced mitochondrial swelling, aggregation and subsequent signaling events leading to necrosis. Similar findings have previously revealed that chemical induction of ROS production in Arabidopsis protoplasts caused a rapid and consistent change in mitochondrial morphology that preceded cell death (Scott and Logan, 2008). Moreover, we showed that *N. benthamiana* necrotic response to MNSV was associated with upregulation of SA-, HR- and oxidative stress-related genes. Although we cannot rule out the possibility that other APX

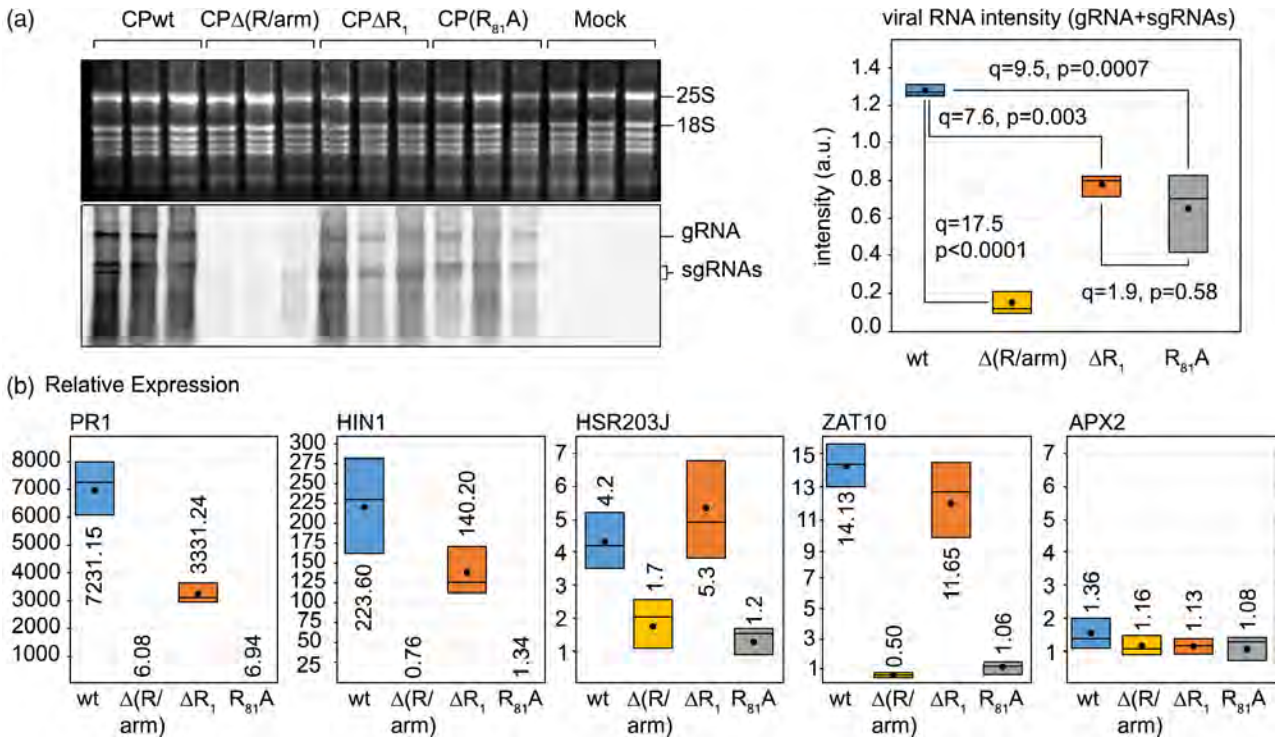

Figure 10. Analysis of *ZAT10, HIN1, HSR203J* and *PR1* gene expression by quantitative real-time reverse transcription polymerase chain reaction (qRT-PCR) in *Nicotiana benthamiana*.

(a) Northern blot to detect melon necrotic spot virus (MNSV) RNAs in MNSV, MNSV-CPR$_1$, MNSV-CP$_{R81A}$ and MNSV-CPΔ(R/arm) inoculated leaves. Ethidium bromide staining of ribosomal RNAs is shown as loading control. RNAs from leaf pools of three independent assays are shown. Boxplot represents the genomic plus subgenomic MNSV RNA band chemiluminescence intensities from three replicates. Points inside boxes represent the mean from three replicates. $P < 0.05$ indicates statistical significance.

(b) Relative expression of *PR1, HIN1, HSR203J* and *ZAT10* genes analyzed by qRT-PCR in RNA samples from leaves inoculated with MNSV and the indicated mutants at 5 days post-inoculation (dpi). Mock corresponds to RNAs from leaves rubbed with inoculation buffer. Boxplots represent the relative expression in three biological replicates. The lower and upper limits of the boxes are plotting the min and max values, respectively, whereas the lines dividing them represent the median values. Points inside boxes represent the mean from the three replicates. $P < 0.05$ indicates statistical significance. CP, coat protein.

isoforms are induced, downregulation of APX activity through transcriptional and translation repression and posttranslational modifications has been described to promote oxidative burst needed for programmed cell death (de Pinto et al., 2012). All these cellular and molecular events together suggest that MNSV-host compatible interaction may result from an inefficient HR that usually does not stop disease progression but reinitiates in newly infected cells. This assumption fits closely with the observed trailing necrosis associated with vascular tissues, including stems, petioles and interveinal regions, occasionally killing the plant (Balint-Kurti, 2019).

Previous studies have suggested that CP mitochondrial and chloroplast targeting may assist, early in infection, CNV uncoating process as both organelles are often found closely associated with peroxisomes, where CNV replicates (Hui et al., 2010). Even if that was true for MNSV, we found experimental evidence suggesting that CP organelle targeting affects later infection stages. MNSV infection initiated by uncoated RNAs was negatively affected when organelle targeting, but not the rest of known CP functions, was impaired in MNSV-CPΔR$_1$. Moreover, MNSV RNA encapsidation was prominent and associated with unprocessed CP presence in non-photosynthetic tissues like roots or stems, where chloroplasts are lacking or fewer than in leaves (Kobayashi and Masuda, 2013; Maksymowych et al., 1993), indicating that virion assembly rate could also be regulated by this mean. To increase genome encapsidation specificity, virion assembly should take place near replication sites. MNSV CP targeting mitochondrial-derived VRCs could provide the most efficient way to bring together the main virion components, CP and viral RNAs. However, we showed that CP behaves like a mitochondrial matrix protein, most likely undergoing R/arm processing and becoming useless for genome binding. One possibility is that the processing rate of mitochondrial cargo could be modulated at some infection stages allowing or not encapsidation from CP mitochondrial pool. In this sense, mitochondrial processing peptidase expression was reported to be down- or upregulated in susceptible and resistant melon, respectively, especially 5 days after infection with the resistance-breaking

MNSV-Mα5/3′264, an MNSV(Al/264)-like chimeric virus (Gómez-Aix et al., 2016).

Apart from that mentioned above, we propose an additional role for MNSV CP, associated with its organelle targeting, in managing the balance between plant defense and virus counter-defense responses leading to a compatible interaction (Table S1). Some plant viruses mitigate symptoms to persist in the host, decreasing the accumulation and/or activity of key viral effectors by genome translation repression, degradation through host pathways and post-translational modification (Paudel and Sanfaçon, 2018). Our results indicated that organelle targeting and processing compromise viral counter-defense as MNSV CP was shown to fulfil its RSS task in the cytoplasm by siRNA sequestration through the R_2/arm region and preventing the spread of systemic silencing (Serra-Soriano et al., 2017). Similarly, TBSV p19 cytoplasmic depletion upon translocation into the nucleus by ALY proteins negatively affects its silencing suppressor activity (Canto et al., 2006). We showed that necrosis induction was p29 dose-dependent, and thus it could be closely linked to high infection levels mediated by antiviral RSS. In this sense, the accumulation of MNSV-CPΔR_1 holding CPΔR_1, which still allows genome binding and encapsidation (Serra-Soriano et al., 2017), has enhanced RSS capacity but fails to localize in both organelles and was negatively affected or impaired at local or systemic level. Although MNSV-CPΔR_1 accumulation was significantly lower than MNSV, the induction of pathogen and HR-related gene markers was in the same order of magnitude. The high levels of CPΔR_1 in the cytoplasm likely enhance viral RSS activity favoring early p29 overaccumulation. Far from improving MNSV replication, this magnifies mitochondrial alteration reinforcing antiviral defense or accelerating its activation as occurs when co-expressing p29 and CPΔR_1. Thus, CP organelle targeting and processing might be considered as a mechanism to avoid excessive RSS activity in green parts where uncoated replicating genomes can spread protected inside motile VRCs but, in turn, could facilitate horizontal transmission through the interaction of vector fungus zoospores with virions accumulated in roots. Remarkably, MNSV accumulation was previously observed to be significantly higher in infected melon roots than in cotyledons or leaves (Gosalvez-Bernal et al., 2008). Melon roots have also been reported as a tissue where RNA silencing occurs (Herranz et al., 2015). This remarkable tissue tropism can now be explained by the lack of CP processing and concomitant RSS activity and virion accumulation in roots observed here.

Our results also indicate that S/P domains, which correspond to organelle mature CP, could mitigate the appearance of necrosis and cytopathic alterations, possibly interfering with plant response. CP, but not R/arm-GFP, expression inhibited p29-induced necrosis when co-expressed at equivalent levels. Induction of stromules was attenuated, and chloroplast-to-nucleus movement and communication were not observed when the whole CP was used. MNSV-CP(R_{81}A), holding CP(R_{81}A), which had reduced suppressor activity but still targets both organelles, accumulated at similar MNSV-CPΔ$_1$ levels but did not induce necrotic lesions nor modify gene marker expression. In contrast, when S/P domains were replaced by GFP in MNSV(R/arm-GFP), the infection was mainly restricted to initially infected cells showing exacerbated cytopathic effects that affected mitochondria and chloroplasts. Some MNSV(R/arm-GFP) foci were observed, suggesting the existence of a rather unstable balance between defense and counter-defense mechanisms that occasionally inclines in favor of progression. Moreover, the number of VRCs significantly increases in MNSV(R/arm-GFP) foci, as happened in MNSV(CPΔR_1-GFP). This situation raises the question of whether mitochondrial morphology changes leading to VRC building are due to a direct effect of p29 on membrane curvature upon recruiting host membrane-deforming proteins, as described for tombusvirus p33 on peroxisome membranes (Nagy, 2016), or indirectly result from membrane potential disruption that makes mitochondria grow into larger structures. These last options could be emphasized in MNSV(R/arm-GFP) by S/P absence and in MNSV (CPΔR_1-GFP) by cytoplasmic location and enhanced RSS activity. Yet still the possibility that host and MNSV work in concert to build VRCs cannot be ruled out.

At the time of writing this manuscript, Alam et al. (2021) published an article about CNV CP targeting addressing part of the objectives described in this work. Similar to MNSV CP, these authors reported that CNV CP targeting the chloroplast stroma inhibits necrosis induced by CNV p33 and TBSV p19, and interferes with host defense response modulating SA signaling pathway. However, previous work by the same group suggested that only 1–5% of the CNV CP is targeted to chloroplast during infection (Xiang et al., 2006). This result contrasts with our observation where both CP and virions were barely detected in leaves during MNSV infection, suggesting a much higher percentage of organelle targeting for MNSV CP than for CNV CP. Therefore, mechanisms controlling the equilibrium to generate a compatible interaction in both pathosystems could not be exactly similar, and most likely rely on the presence in CNV of a TBSV p19-like silencing suppressor, p20, that is absent in gammacarmoviruses (Hao et al., 2011). Whether MNSV CP organelle targeting function is beyond a self-attenuation mechanism to not prematurely harm the plant host or has a more direct implication interfering with antiviral plant signaling starting in mitochondria and chloroplasts needs further investigation.

In summary, cytoplasmic and organellar CP could be similar to echoproteins, a term that refers to identical or nearly identical proteins, having different functions in different subcellular compartments (Yogev et al., 2011). On the one hand,

proteolytic processing of CP after targeting mitochondria and chloroplasts could result in two CP-derived peptides, both of them unsuitable for RSS and genome encapsidation. The overaccumulation of the split R/arm region could be perceived as a signal molecule for danger acting then as an elicitor, whereas the rest of the CP (S/P domains) could be considered as an effector interfering with plant defence signaling starting in these organelles. On the other hand, after reaching a certain threshold of viral replication, the organellar targeting of the CP could be prevented, for example, by masking dTP through interactions with other CP molecules or different viral and host proteins, giving rise to a subpopulation of non-processed cytoplasmic CP suitable to function in RSS and genome encapsidation.

EXPERIMENTAL PROCEDURES

Molecular cloning

For subcellular localization studies using an agro-mediated transient expression, MNSV CP, CP mutant (Figure S2) and p29 ORFs were PCR-amplified from available clones (Serra-Soriano et al., 2017), digested and fused in-frame to the 5′ or 3′ ends of GFP by cloning them into a modified pBluescript including the CaMV 35Sx2 promoter and PoPit terminator. p29 ORF was also fused in-frame to the 5′ or 3′ ends of ChFP. Next, CP, all CP mutant and p29 expression cassettes were liberated by *Sac*I or *Hind*III digestion, respectively, to be cloned into pMOG800 (Knoester et al., 1998). For subcellular localization studies during MNSV infection, pMNSV(AI) (Genoves et al., 2006) was modified by replacing its 3′-UTR from that of MNSV-264 isolate (Díaz et al., 2004) generating pMNSV(AI/264). pMNSV(CP-GFP) and pMNSV(CP-HA) were obtained by linearizing pMNSV(AI/264) by inverse PCR and cloning either *GFP* or HA after *CP* using type IIs BveI restriction enzyme. pMNSV(CP$\Delta R_{1[6-30]}$-GFP), pMNSV(CP$\Delta R_{1[6-30]}$-HA) and pMNSV(R/arm-GFP) were generated by deletion of positions 6–30 of R_1 subdomain or S/P domains in pMNSV(CP-GFP) or pMNSV(CP-HA), as appropriate, by inverse PCR and self-ligation through cohesive *Bve*I ends. For MNSV infection studies in *N. benthamiana*, pMNSV(AI/264) was the basis to introduce R/arm, R, arm, R_1, R_2 and R_2/arm deletions by inverse PCR and self-ligation through cohesive *Bve*I ends. To obtain the R_1/arm deletion mutant, the arm region was deleted from pMNSV(CPΔR1) following the same procedure as before. R_{81}A point-mutation was introduced in pMNSV(AI/264) by inverse PCR using complementary primers. A TRV expression system was used for CP-HA/ChFP expression in leaves, stems and roots (MacFarlane and Popovich, 2000). For this purpose, C-terminal HA-tagged CP and ChFP ORFs were combined with pea early-browning virus (PEBV) CP subgenomic promoter by overlapping PCR and cloned into pTRV2 using Gateway technology (Liu et al., 2002). Vectors were named TRV2$_{promPEBV}$[CP-HA] and TRV2$_{promPEBV}$[ChFP], respectively. Additionally, the AMV RNA 3 expression system (Martínez-Pérez et al., 2019) was used to compare the silencing suppressor capacity between CP and CPΔR_1. Both proteins were cloned under the control of a duplicated RNA4 subgenomic promoter into a modified RNA3 vector using appropriate restriction enzymes (Sanchez-Navarro et al., 2001). The oligonucleotides used are listed in Table S3.

Subcellular fluorescent markers

Transit peptides of yeast cytochrome oxidase subunit IV (coxP, matrix; Köhler et al., 1997) and Arabidopsis glycyl-tRNA synthetase (glyrsP, stroma and matrix; Duchêne et al., 2001), as well as the chloroplastic *N. benthamiana* proteins, magnesium-protoporphyrin IX chelatase H subunit (CHLH/ABAR, outer envelope; Shang et al., 2010), N receptor-interacting protein 1 (NRIP1, stroma; Caplan et al., 2008) and chloroplast unusual positioning1 (CHUP1, outer envelope; Oikawa et al., 2008) were RT-PCR amplified from corresponding total RNAs and fused to fluorescent protein N-terminus following the same procedure described above. Markers obtained were designed as coxP-ChFP, glyrsP-ChFP/GFP, ABAR-ChFP, NRIP1-ChFP and CHUP1-ChFP, respectively. Besides, the HIV-1 Rev NES was fused to NRIP1ChFP N-terminus ($_{NES}$NRIP1-ChFP), including the corresponding sequence in the forward primer. The oligonucleotides used are listed in Table S3.

Protein expression and Western blot analysis

Transient expression of proteins from binary vectors was performed using the *Agrobacterium tumefaciens* (C58C1) infiltration method in *N. benthamiana*. Overnight transformed bacteria cultures were collected and adjusted to an OD_{600} of 0.2 with 10 mM $MgCl_2$, 10 mM 2-(N-morpholino)ethanesulfonic acid pH 5.6 and 150 μM acetosyringone. These suspensions were introduced in 4-week-old leaves by infiltration into the abaxial side. For experiments requiring co-expression of two proteins, bacterial cultures were mixed before infiltration. Fluorescence was visualized at 48 hpi using confocal microscopy. For TRV-mediated expression, pTRV1 in combination with TRV2$_{promPEBV}$[CP-HA] or TRV2$_{promPEBV}$[ChFP] bacterial cultures were adjusted to an OD_{600} of 1 and mixed before infiltration. Plants were kept in growth chambers at 16 h light, 25°C, and 8 h dark, 22°C. Two weeks after infiltration, ChFP fluorescence was visualized under UV light using a rhodamine filter in a Leica MZ16 fluorescence stereomicroscope. For Western blot analysis, proteins were extracted from 100 mg of fresh tissue using 500 μl of Laemmli buffer, and crude extracts clarified by centrifugation. After heat denaturing, 10 μl of each extract was analyzed by polyacrylamide gel electrophoresis and wet-transferred to polyvinylidene difluoride membranes. Immunodetection was performed using a monoclonal antibody against GFP C-terminus or HA epitope. Blots were developed by chemiluminescence and examined using a Fujifilm LAS-3000 Imager. Densitometry was performed using Fujifilm Image Gauge V4.0.

CLSM, image processing and statistical analysis

Subcellular localization analysis was conducted with an inverted Zeiss LSM 780 confocal microscope. eGFP and ChFP fluorescence were imagined by 488 and 561 nm laser excitation, respectively. The corresponding emission detection windows were 492–532 and 590–630, respectively. The chlorophyll excitation wavelength was 488 nm, and fluorescence was detected above 700 nm. Image processing and analysis, including overlays, Z-stack projections, movies, and estimation of p29 cluster sizes and areas, was performed using FIJI (Schindelin et al., 2012) or ZEN 2011. Quantification of the stromule induction was done in epidermal cells marked with NRIP1-ChFP. Maximum intensity two-dimensional projections of 30 Z-stack slices were taken by confocal microscopy, each one including 5–6 cells (n = 10, three replicates). Stromules and chloroplasts were counted using the MiToBo Cell Counter plugin of FIJI. Stromule induction was calculated as the number of chloroplasts with stromules per total chloroplast number. Statistical significances at the 95% confidence level (α = 0.05) were determined using Graphpad Prism ($P < 0.05$) through unpaired parametric t-test with Welch's correction as well as one-way analysis of variance and Tukey's *post-hoc* test for multiple comparisons.

Virus inoculation

The GFP-recombinant, wild-type and mutated MNSV transcripts were synthesized *in vitro* using *Pst*I-linearized vectors. Transcripts were quantified and used to infect 2-week-old *N. benthamiana* plants by rubbing them on leaves (4–5 μg per leaf) with phosphate buffer (30 mM, pH 7.0) and carborundum. For subcellular studies, each RNA variant was inoculated in three leaves from three different plants. For infectivity studies, 10 plants per RNA variant were inoculated. Three independent replicates were made, leaving some time between them. Plants were grown under long-day photoperiods as described above.

Total RNA extraction and Northern blot analysis

For Northern blot, total RNA was isolated with RiboZol RNA Extraction Reagent Samples, electrophoresed on a denaturing gel (1 × 3-(N-morpholino)propanesulfonic acid, 5% formaldehyde, 1.3% agarose) and capillary-transferred to nylon membranes in 10 × SSC (1.5 M NaCl, 0.15 M sodium citrate). For dot blot, nucleic acids were isolated using the Dellaporta method (Dellaporta et al., 1983) and spotted (300 ng) onto nylon membranes. Hybridization was performed using a digoxigenin-labeled riboprobe against MNSV CP or p29. Viral RNA detection was conducted using CSPD chemiluminescent substrate and Fujifilm LAS-3000 Imager. Densitometry was performed using Fujifilm Image Gauge V4.0.

Virion purification

Two weeks after MNSV(AI/264) RNA inoculation, 10 g of stems/petioles, systemic leaves or roots was collected and homogenized in liquid nitrogen. The frozen powder was dissolved in 0.2 M sodium acetate, pH 5.0 and centrifuged at 7700 ***g***. After supernatant filtering, virions were pelleted by centrifugation at 146 000 ***g*** for 2 h through a 20% sucrose cushion and resuspended in 50 μl of 10 mM Tris-HCl, pH 7.3. For virions analysis, samples were electrophoresed (40 mM Tris-acetate, 1 mM EDTA, pH 8.0, agarose 1%), transferred to nylon membranes, and analyzed as described before. Three independent replicates were performed.

qRT-PCR

DNase I treatment was performed to remove genomic DNA from RNA samples. First-strand cDNA was synthesized from 0.5 μg of total RNA using RevertAid H Minus Reverse Transcriptase and specific oligonucleotides (Table S3). qRT-PCR was carried out with the ABI 7500 Fast Real-Time PCR detection system using PyroTaq EvaGreen qPCR Supermix, specific oligonucleotides and recommended qPCR cycles. Specific oligonucleotides were designed using Primer3Web 4.1.0. Oligonucleotide efficiencies were tested by qRT-PCR using 10-fold serial dilutions of the corresponding cDNA. MNSV-inoculated leaf samples from 10 plants per each analyzed construct were pooled per assay generating three biological replicates. Each biological replicate was run in triplicate. Three reference genes encoding the elongation factor 1-α (*EF1α*, TC19582), F-BOX family protein (*F-BOX*, Niben.v0.3. Ctg24993647) and Protein phosphatase 2A (*PP2A*, TC21939) were used to normalize the expression levels (Liu et al., 2012). The samples from Mock inoculated plants were used as control.

ACKNOWLEDGEMENTS

The authors thank L. Corachan-Valencia for technical assistance. This work was funded by grant BIO2017–88321-R from the Spanish Agencia Estatal de Investigación (AEI) and Fondo Europeo de Desarrollo Regional (FEDER). J.A.N. and M.S.-B. are the recipients of a postdoctoral contract and a PhD fellowship from the Ministerio de Ciencia, Innovación y Universidades of Spain, respectively.

Ministerio de Ciencia e Innovación (PID2020-115571RB-I00), European Regional Development Fund

AUTHOR CONTRIBUTIONS

JAN and VP conceived and designed the experiments. JAN, MS-B and JAS-N performed the experiments. JAN analyzed the data. JAN and VP wrote the manuscript. All authors reviewed and edited the manuscript.

CONFLICTS OF INTEREST

The authors confirm that there is no conflict of interest to declare.

DATA AVAILABILITY STATEMENT

All relevant data can be found within the manuscript and its supporting materials.

SUPPORTING INFORMATION

Additional Supporting Information may be found in the online version of this article.

Figure S1. Subcellular localization of five CPs from members of the genus *Tombusvirus*.

Figure S2. Multiple amino acid sequence alignment of the CP N-terminal regions of MNSV and 16 members of genus *Tombusvirus* and helical wheel presentation of some amphipathic α-helices in the N-terminal regions of MNSV and *Tombusvirus* CPs.

Figure S3. Schematic representation of the MNSV CP domains (R, arm, S and P) and mutants used in this study.

Figure S4. Co-expression of $_{NES}$NRIP1-ChFP with GFP, CPΔ(R/arm)-GFP, glyrsP-GFP and R/arm-GFP.

Figure S5. Amino acid composition of the MNSV CP R_1, R_2 and arm regions.

Figure S6. Subcellular localization of the MNSV CP deletion mutants fused to the GFP C terminus in leaves of *N. benthamiana* at 48 hpi.

Figure S7. Western blot analysis of the GFP-tagged MNSV CP and deletion mutants transiently expressed in leaves of *N. benthamiana*.

Figure S8. Effect of CP mutations on MNSV infectivity in *N. benthamiana*.

Table S1. Functions of the different domains of MNSV CP

Table S2. Prediction of the subcellular localization of MNSV CP and 18 tombusvirus CPs

Table S3. List of oligonucleotides used in this study

Movie S1. Time-lapse series showing the movement of CP-GFP-labeled mitochondria at 48 hpi in an epidermal cell of *N. benthamiana*.

Movie S2. 360° 3D reconstruction of Figure 5(a) showing an MNSV (CP-GFP) infection focus at 5 dpi in *N. benthamiana*.

Movie S3. Time-lapse series showing the movement of CP-GFP-labeled round structures at 48 hpi in epidermal cells of *N. benthamiana*.

Movie S4. Z-stack movie showing that juxtanuclear structures consisted of a large cluster of size-heterogeneous p29-GFP labeled vesicles.

Movie S5. 360° 3D reconstruction of Figure 6(g) showing an MNSV(CPΔR_1-GFP) infection focus at 5 dpi in *N. benthamiana*.

REFERENCES

AbuQamar, S., Chen, X., Dhawan, R., Bluhm, B., Salmeron, J., Lam, S. *et al.* (2006) Expression profiling and mutant analysis reveals complex regulatory networks involved in Arabidopsis response to *Botrytis* infection. *The Plant Journal*, **48**, 28–44.

Alam, S.B., Reade, R., Maghodia, A.B., Ghoshal, B., Theilmann, J. & Rochon, D.A. (2021) Targeting of cucumber necrosis virus coat protein to the chloroplast stroma attenuates host defense response. *Virology*, **554**, 106–119.

Balint-Kurti, P. (2019) The plant hypersensitive response: concepts, control and consequences. *Molecular Plant Pathology*, **20**, 1163–1178.

Berglund, A.K., Spånning, E., Biverstål, H., Maddalo, G., Tellgren-Roth, C., Mäler, L. *et al.* (2009) Dual targeting to mitochondria and chloroplasts: characterization of Thr-tRNA synthetase targeting peptide. *Molecular Plant*, **2**, 1298–1309.

Betsuyaku S., Katou S., Takebayashi Y., Sakakibara H., Nomura N. & Fukuda H. (2018) Salicylic acid and jasmonic acid pathways are activated in spatially different domains around the infection site during effector-triggered immunity in Arabidopsis thaliana. *Plant and Cell Physiology*, **59**, 8–16.

Briesemeister, S., Rahnenführer, J. & Kohlbacher, O. (2010) YLoc—an interpretable web server for predicting subcellular localization. *Nucleic Acids Research*, **38**, 497–502.

Burgyán, J., Hornyik, C., Szittya, G., Silhavy, D. & Bisztray, G. (2000) The ORF1 products of tombusviruses play a crucial role in lethal necrosis of virus-infected plants. *Journal of Virology*, **74**, 10873–10881.

Canto, T., Uhrig, J.F., Swanson, M., Wright, K.M. & MacFarlane, S.A. (2006) Translocation of tomato bushy stunt virus P19 protein into the nucleus by ALY proteins compromises its silencing suppressor activity. *Journal of Virology*, **80**, 9064–9072.

Caplan, J.L., Kumar, A.S., Park, E., Padmanabhan, M.S., Hoban, K., Modla, S. *et al.* (2015) Chloroplast stromules function during innate immunity. *Developmental Cell*, **34**, 45–57.

Caplan, J.L., Mamillapalli, P., Burch-Smith, T.M., Czymmek, K. & Dinesh-Kumar, S.P. (2008) Chloroplastic protein NRIP1 mediates innate immune receptor recognition of a viral effector. *Cell*, **132**, 449–462.

Caverzan, A., Passaia, G., Rosa, S.B., Ribeiro, C.W., Lazzarotto, F. & Margis-Pinheiro, M. (2012) Plant responses to stresses: role of ascorbate peroxidase in the antioxidant protection. *Genetics and Molecular Biology*, **35**, 1011–1019.

Chaudhary, A. & Yadav, R.D. (2019) A review on virus protein self-assembly. *Journal of Nanoparticle Research*, **21**, 254.

de Pinto, M.C., Locato, V. & de Gara, L. (2012) Redox regulation in plant programmed cell death. *Plant, Cell and Environment*, **35**, 234–244.

Dellaporta, S.L., Wood, J. & Hicks, J.B. (1983) A plant DNA minipreparation: version II. *Plant Molecular Biology Report*, **1**, 19–21.

Díaz, J.A., Nieto, C., Moriones, E., Truniger, V. & Aranda, M.A. (2004) Molecular characterization of a melon necrotic spot virus strain that overcomes the resistance in melon and nonhost plants. *Molecular Plant–Microbe Interactions*, **17**, 668–675.

Ding, X., Jimenez-Gongora, T., Krenz, B. & Lozano-Duran, R. (2019) Chloroplast clustering around the nucleus is a general response to pathogen perception in *Nicotiana benthamiana*. *Molecular Plant Pathology*, **20**, 1298–1306.

Drozdetskiy, A., Cole, C., Procter, J. & Barton, G.J. (2015) JPred4: a protein secondary structure prediction server. *Nucleic Acids Research*, **43**, 389–394.

Duchêne, A.M., Peeters, N., Dietrich, A., Cosset, A., Small, I.D. & Wintz, H. (2001) Overlapping destinations for two dual targeted glycyl-tRNA synthetases in *Arabidopsis thaliana* and *Phaseolus vulgaris*. *Journal of Biological Chemistry*, **276**, 15275–15283.

Fernández-Crespo, E., Navarro, J.A., Serra-Soriano, M., Finiti, I., García-Agustín, P., Pallás, V. & et al. (2017) Hexanoic acid treatment prevents systemic MNSV movement in *Cucumis melo* plants by priming callose deposition correlating SA and OPDA accumulation. *Frontiers in Plant Science*, **8**, 1793.

Fister, A.S., Mejia, L.C., Zhang, Y., Herre, E.A., Maximova, S.N. & Guiltinan, M.J. (2016) Theobroma cacao L. pathogenesis-related gene tandem array members show diverse expression dynamics in response to pathogen colonization. *BMC Genomics*, **17**, 363.

Fujita, Y., Fujita, M., Yamaguchi-Shinozaki, K. & Director, K. (2009) Transcription factors involved in the crosstalk between abiotic and biotic stress-signaling networks. In: Yoshioka, K. & Shinozaki, K. (Eds.) *Signal crosstalk in plant stress responses*. Hoboken: Wiley-Blackwell, pp. 43–58.

Gautier, R., Douguet, D., Antonny, B. & Drin, G. (2008) HELIQUEST: a web server to screen sequences with specific alpha-helical properties. *Bioinformatics*, **24**, 2101–2102.

Ge, C., Spånning, E., Glaser, E. & Wieslander, Å. (2014) Import determinants of organelle-specific and dual targeting peptides of mitochondria and chloroplasts in *Arabidopsis thaliana*. *Molecular Plant*, **7**, 121–136.

Genoves, A., Navarro, J.A. & Pallas, V. (2006) Functional analysis of the five melon necrotic spot virus genome-encoded proteins. *Journal of General Virology*, **87**, 2371–2380.

Ghoshal, K., Theilmann, J., Reade, R., Maghodia, A. & Rochon, D. (2015) Encapsidation of host RNAs by cucumber necrosis virus coat protein during both agroinfiltration and infection. *Journal of Virology*, **89**, 10748–10761.

Gomez-Aix, C., García-García, M., Aranda, M.A. & Sanchez-Pina, M.A. (2015) Melon necrotic spot virus replication occurs in association with altered mitochondria. *Molecular Plant–Microbe Interactions*, **28**, 387–397.

Gómez-Aix, C., Pascual, L., Cañizares, J., Sánchez-Pina, M.A. & Aranda, M.A. (2016) Transcriptomic profiling of melon necrotic spot virus-infected melon plants revealed virus strain and plant cultivar-specific alterations. *BMC Genomics*, **17**, 429.

Gopalan, S., Wei, W. & He, S.Y. (1996) hrp gene-dependent induction of hin1: a plant gene activated rapidly by both harpins and the avrPto gene-mediated signal. *The Plant Journal*, **10**, 591–600.

Gosalvez-Bernal, B., Genoves, A., Navarro, J.A., Pallas, V. & Sanchez-Pina, M.A. (2008) Distribution and pathway for phloem-dependent movement of Melon necrotic spot virus in melon plants. *Molecular Plant Pathology*, **9**, 447–461.

Hanson, M.R. & Hines, K.M. (2018) Stromules: probing formation and function. *Plant Physiology*, **176**, 128–137.

Hao, X., Lu, A., Sokal, N., Bhagwat, B., Leung, E., Mao, R. *et al.* (2011) Cucumber necrosis virus p20 is a viral suppressor of RNA silencing. *Virus Research*, **155**, 423–432.

Heath, M.C. (2000) Hypersensitive response-related death. *Plant Molecular Biology*, **44**, 321–334.

Hernández, J.A., Gullner, G., Clemente-Moreno, M.J., Künstler, A., Juhász, C., Díaz-Vivancos, P. *et al.* (2016) Oxidative stress and antioxidative responses in plant–virus interactions. *Physiological and Molecular Plant Pathology*, **94**, 134–148.

Herranz, M.C., Navarro, J.A., Sommen, E. & Pallas, V. (2015) Comparative analysis among the small RNA populations of source, sink and conductive tissues in two different plant-virus pathosystems. *BMC Genomics*, **16**, 117.

Horton, P., Park, K.-J., Obayashi, T., Fujita, N., Harada, H., Adams-Collier, C.J. *et al.* (2007) WoLF PSORT: protein localization predictor. *Nucleic Acids Research*, **35**, 585–587.

Hui, E., Xiang, Y. & Rochon, D. (2010) Distinct regions at the N-terminus of the cucumber necrosis virus coat protein target chloroplasts and mitochondria. *Virus Research*, **153**, 8–19.

Jin, X., Cao, X., Wang, X., Jiang, J., Wan, J., Laliberté, J.-F. & et al. (2018) Three-dimensional architecture and biogenesis of membrane structures associated with plant virus replication. *Frontiers in Plant Science*, **9**, 57.

Kmiec, B., Teixeira, P.F. & Glaser, E. (2014) Shredding the signal: targeting peptide degradation in mitochondria and chloroplasts. *Trends in Plant Science*, **19**, 771–778.

Knoester, M., van Loon, L.C., van den Heuvel, J., Hennig, J., Bol, J.F. & Linthorst, H.J.M. (1998) Ethylene-insensitive tobacco lacks nonhost resistance against soil-borne fungi. *Proceedings of the National Academy of Sciences United States of America*, **95**, 1933–1937.

Kobayashi, K. & Masuda, T. (2013) Spatial and temporal regulation of chloroplast development in arabidopsis root. In: Kuang, T., Lu, C. & Zhang, L. (Eds.) *Photosynthesis research for food, fuel and the future*. Berlin, Heidelberg: Springer, pp. 389–393.

Köhler, R.H., Zipfel, W.R., Webb, W.W. & Hanson, M.R. (1997) The green fluorescent protein as a marker to visualize plant mitochondria in vivo. *The Plant Journal*, **11**, 613–621.

Krenz, B., Jeske, H. & Kleinow, T. (2012) The induction of stromule formation by a plant DNA-virus in epidermal leaf tissues suggests a novel

intra- and intercellular macromolecular trafficking route. *Frontiers in Plant Science*, **3**, 291.

Laliberté, J.-F. & Sanfaçon, H. (2010) Cellular remodeling during plant virus infection. *Annual review of Phytopathology*, **48**, 69–91.

Laliberté, J.-F. & Zheng, H. (2014) Viral manipulation of plant host membranes. *Annual Review of Virology*, **1**, 237–259.

Li, W., Xu, Y.P., Zhang, Z.X., Cao, W.Y., Li, F., Zhou, X. *et al.* (2012) Identification of genes required for nonhost resistance to *Xanthomonas oryzae* pv. *oryzae* reveals novel signaling components. *PLoS One*, **7**, e42796.

Li, Y., Cui, H., Cui, X. & Wang, A. (2016) The altered photosynthetic machinery during compatible virus infection. *Current Opinion in Virology*, **17**, 19–24.

Liu, D., Shi, L., Han, C., Yu, J., Li, D. & Zhang, Y. (2012) Validation of reference genes for gene expression studies in virus-infected *Nicotiana benthamiana* using quantitative real-time PCR. *PLoS One*, **7**(9), e46451.

Liu, Y., Lan, X., Song, S., Yin, L., Dry, I.B., Qu, J. *et al.* (2018) In planta functional analysis and subcellular localization of the oomycete pathogen *Plasmopara viticola* candidate RXLR effector repertoire. *Frontiers in Plant Science*, **9**, 286.

Liu, Y., Schiff, M. & Dinesh-Kumar, S.P. (2002) Virus-induced gene silencing in tomato. *The Plant Journal*, **31**, 777–786.

Loebenstein, G. (2009) Local lesions and induced resistance. *Advances in Virus Research*. **75**, 73–117.

MacFarlane, S. & Popovich, A. (2000) Efficient expression of foreign proteins in roots from *Tobravirus* vectors. *Virology*, **267**, 29–35.

Maksymowych, R., Dollahon, N., di Cola, L.P. & Orkwiszewski, J.A.J. (1993) Chloroplasts in tissues of some herbaceous stems. *Acta Societatis Botanicorum Poloniae*, **62**, 123–126.

Martínez-Pérez, M., Navarro, J.A., Pallás, V. & Sánchez-Navarro, J.A. (2019) A sensitive and rapid RNA silencing suppressor activity assay based on alfalfa mosaic virus expression vector. *Virus Research*, **272**, 197733.

Miras, M., Torre, C., Gómez-Aix, C., Hernando, Y. & Aranda, M.A. (2020) Development of monoclonal antibodies against melon necrotic spot virus and their use for virus detection. *Journal of Virological Methods*, **278**, 113837.

Miyazono, Y., Hirashima, S., Ishihara, N., Kusukawa, J., Nakamura, K.I. & Ohta, K. (2018) Uncoupled mitochondria quickly shorten along their long axis to form indented spheroids, instead of rings, in a fission-independent manner. *Scientific Reports*, **8**, 1–14.

Mochizuki, T., Hirai, K., Kanda, A., Ohnishi, J., Ohki, T. & Tsuda, S. (2009) Induction of necrosis via mitochondrial targeting of melon necrotic spot virus replication protein p29 by its second transmembrane domain. *Virology*, **390**, 239–249.

Mur, L.A.J.J., Kenton, P., Lloyd, A.J., Ougham, H. & Prats, E. (2007) The hypersensitive response; the centenary is upon us but how much do we know? *Journal of Experimental Botany*, **59**, 501–520.

Nagy, P.D. (2016) Tombusvirus-host interactions: co-opted evolutionarily conserved host factors take center court. *Annual Review of Virology*, **3**, 491–515.

Nott, A., Jung, H.-S., Koussevitzky, S. & Chory, J. (2006) Plastid-to-nucleus retrograde signaling. *Annual Review of Plant Biology*, **57**, 739–759.

Ohki, T., Akita, F., Mochizuki, T., Kanda, A., Sasaya, T. & Tsuda, S. (2010) The protruding domain of the coat protein of melon necrotic spot virus is involved in compatibility with and transmission by the fungal vector *Olpidium bornovanus*. *Virology*, **402**, 129–134.

Ohki, T., Sako, I., Kanda, A., Mochizuki, T., Honda, Y. & Tsuda, S. (2008) A new strain of melon necrotic spot virus that is unable to systemically infect *Cucumis melo*. *Phytopathology*, **98**, 1165–1170.

Oikawa, K., Yamasato, A., Kong, S.G., Kasahara, M., Nakai, M., Takahashi, F. *et al.* (2008) Chloroplast outer envelope protein Chup1 is essential for chloroplast anchorage to the plasma membrane and chloroplast movement. *Plant Physiology*, **148**, 829–842.

Pallas, V. & García, J.A. (2011) How do plant viruses induce disease? Interactions and interference with host components. *Journal of General Virology*, **92**, 2691–2705.

Paudel, D.B. & Sanfaçon, H. (2018) Exploring the diversity of mechanisms associated with plant tolerance to virus infection. *Frontiers in Plant Science*, **9**, 1575.

Perello, C., Llamas, E., Burlat, V., Ortiz-Alcaide, M., Phillips, M.A., Pulido, P. *et al.* (2016) Differential subplastidial localization and turnover of enzymes involved in isoprenoid biosynthesis in chloroplasts. *PLoS One*, **11**, e0150539.

Petre, B., Saunders, D.G.O., Sklenar, J., Lorrain, C., Win, J., Duplessis, S. *et al.* (2015) Candidate effector proteins of the rust pathogen *Melampsora larici-populina* target diverse plant cell compartments. *Molecular Plant–Microbe Interactions*, **28**, 689–700.

Pontier, D., Tronchet, M., Rogowsky, P., Lam, E. & Roby, D. (1998) Activation of hsr203, a plant gene expressed during incompatible plant-pathogen interactions, is correlated with programmed cell death. *Molecular Plant-Microbe Interactions*, **11**, 544–554.

Pujol, C., Maréchal-Drouard, L. & Duchêne, A.M. (2007) How can organellar protein N-terminal sequences be dual targeting signals? In silico analysis and mutagenesis approach. *Journal of Molecular Biology*, **369**, 356–367.

Ralph, S.A., Foth, B.J., Hall, N. & McFadden, G.I. (2004) Evolutionary pressures on apicoplast transit peptides. *Molecular Biology and Evolution*, **21**, 2183–2194.

Reape, T.J., Brogan, N.P. & McCabe, P.F. (2015) Mitochondrion and chloroplast regulation of plant programmed cell death. In: Gunawardena, A. & McCabe, P. (Eds.) *Plant programmed cell death*. Cham: Springer, pp. 33–53.

Riviere, C.J., Pot, J., Tremaine, J.H. & Rochon, D.M. (1989) Coat protein of melon necrotic spot *Carmovirus* is more similar to those of tombusviruses than those of carmoviruses. *Journal of General Virology*, **70**, 3033–3042.

Rochon, D., Singh, B., Reade, R., Theilmann, J., Ghoshal, K., Alam, S.B. *et al.* (2014) The p33 auxiliary replicase protein of Cucumber necrosis virus targets peroxisomes and infection induces de novo peroxisome formation from the endoplasmic reticulum. *Virology*, **452–453**, 133–142.

Rossel, J.B., Wilson, P.B., Hussain, D. *et al.* (2007) Systemic and intracellular responses to photooxidative stress in Arabidopsis. *The Plant Cell*, **19**, 4091–4110.

Sanchez-Navarro, J., Miglino, R., Ragozzino, A. & Bol, J.F. (2001) Engineering of alfalfa mosaic virus RNA 3 into an expression vector. *Archives of Virology*, **146**, 923–939.

Schindelin, J., Arganda-Carreras, I., Frise, E., Kaynig, V., Longair, M., Pietzsch, T. *et al.* (2012) Fiji: an open-source platform for biological-image analysis. *Nature Methods*, **9**, 676–682.

Scott, I. & Logan, D.C. (2008) Mitochondrial morphology transition is an early indicator of subsequent cell death in Arabidopsis. *New Phytologist*, **177**, 90–101.

Serra-Soriano, M., Navarro, J.A., Genoves, A. & Pallás, V. (2015) Comparative proteomic analysis of melon phloem exudates in response to viral infection. *Journal of Proteomics*, **124**, 11–24.

Serra-Soriano, M., Navarro, J.A. & Pallas, V. (2017) Dissecting the multifunctional role of the N-terminal domain of the melon necrotic spot virus coat protein in RNA packaging, viral movement and interference with antiviral plant defence. *Molecular Plant Pathology*, **18**, 837–849.

Shang, Y., Yan, L., Liu, Z.Q. *et al.* (2010) The Mg-chelatase H subunit of Arabidopsis antagonizes a group of WRKY transcription repressors to relieve ABA-responsive genes of inhibition. *The Plant Cell*, **22**, 1909–1935.

Shen, B.R., Zhu, C.H., Yao, Z., Cui, L.L., Zhang, J.J., Yang, C.W. *et al.* (2017) An optimized transit peptide for effective targeting of diverse foreign proteins into chloroplasts in rice. *Scientific Reports*, **7**, 1–12.

Sperschneider, J., Catanzariti, A.M., Deboer, K., Petre, B., Gardiner, D.M., Singh, K.B. *et al.* (2017) LOCALIZER: subcellular localization prediction of both plant and effector proteins in the plant cell. *Scientific Reports*, **7**(1), 44598.

Su, T., Li, W., Wang, P. & Ma, C. (2019) Dynamics of peroxisome homeostasis and its role in stress response and signaling in plants. *Frontiers in Plant Science*, **10**, 705.

Tanz, S.K., Castleden, I., Small, I.D. & Harvey Millar, A. (2013) Fluorescent protein tagging as a tool to define the subcellular distribution of proteins in plants. *Frontiers in Plant Science*, **4**, 214.

van Aken, O. & van Breusegem, F. (2015) Licensed to kill: mitochondria, chloroplasts, and cell death. *Trends in Plant Science*, **20**, 754–766.

van Loon, L.C. (1997) Induced resistance in plants and the role of pathogenesis-related proteins. *European Journal of Plant Pathology*, **103**, 753–765.

Verchot, J. (2016) How does the stressed out ER find relief during virus infection? *Current Opinion in Virology*, **17**, 74–79.

Wada, Y., Tanaka, H., Yamashita, E., Kubo, C., Ichiki-Uehara, T., Nakazono-Nagaoka, E. *et al.* (2008) The structure of melon necrotic spot virus determined at 2.8 Å resolution. *Acta Crystallographica Section F Structural Biology and Crystallization Communications*, **64**, 8–13.

Wan, J., Cabanillas, D.G., Zheng, H. & Laliberte, J.-F. (2015) Turnip mosaic virus moves systemically through both phloem and xylem as membrane-associated complexes. *Plant Physiology*, **167**, 1374–1388.

Wang, Y., Selinski, J., Mao, C., Zhu, Y., Berkowitz, O., Whelan, J. *et al.* (2020) Linking mitochondrial and chloroplast retrograde signalling in plants. *Philosophical Transactions of the Royal Society Series B, Biological Sciences*, **375**. https://doi.org/10.1098/rstb.2019.0410

Xiang, Y., Kakani, K., Reade, R., Hui, E. & Rochon, D. (2006) A 38-amino-acid sequence encompassing the arm domain of the cucumber necrosis virus coat protein functions as a chloroplast transit peptide in infected plants. *Journal of Virology*, **80**, 7952–7964.

Yang F., Xiao K., Pan H. & Liu J. (2021) Chloroplast: the emerging battlefield in plant–microbe interactions. *Frontiers in Plant Science*, **12**. http://dx.doi.org/10.3389/fpls.2021.637853

Yogev, O., Naamati, A. & Pines, O. (2011) Fumarase: a paradigm of dual targeting and dual localized functions. *FEBS Journal*, **278**, 4230–4242.

Zhao, J., Zhang, X., Hong, Y. & Liu, Y. (2016) Chloroplast in plant–virus interaction. *Frontiers in Microbiology*, **7**, 1565.